NASA CR-156669

SQT

dynatherm
CORPORATION

DTM-73-7

TECHNICAL SUMMARY REPORT

for

HEAT PIPE DEVELOPMENT

July 31, 1973

Prepared under Contract NAS5-11455

by

Dynatherm Corporation
One Industry Lane
Cockeysville, Maryland

for

National Aeronautics and Space Administration
Goddard Space Flight Center

FOREWORD

This technical report describes the work performed for the National Aeronautics and Space Administration under Contract NAS5-11455, entitled "Heat Pipe Development." The program was administered by Goddard Space Flight Center, Greenbelt, Maryland, with Dr. John B. Schutt as the NASA Technical Officer. The work was performed by Dynatherm Corporation, Cockeysville, Maryland, with Dr. Walter Bienert serving as Program Manager and Principal Investigator.

Several people contributed to the technical work described in this report. Messrs. H. Fox and N. Lee formulated the analytical model and, with the assistance of Mr. J. Liles, conducted most of the tests. Special thanks are accorded to Dr. Schutt of GSFC for his participation in many discussions and for his overall support during the program.

ABSTRACT

The objective of this program was to investigate analytically and experimentally the performance of heat pipes with composite wicks -- specifically, those having pedestal arteries and screwthread circumferential grooves. An analytical model was developed to describe the effects of screwthreads and screen secondary wicks on the transport capability of the artery. The model describes the hydrodynamics of the circumferential flow in triangular grooves with azimuthally varying capillary menisci and liquid cross-sections. Normalized results were obtained which give the influence of evaporator heat flux on the axial heat transport capability of the arterial wick. In order to evaluate the priming behavior of composite wicks under actual load conditions, an "inverted" glass heat pipe was designed and constructed. In the inverted heat pipe, the wick structure is attached to the outside of a metal tube and heat source and heat sink are located inside. The tube and wick are surrounded by a glass pipe which provides the vapor space. Priming and depriming, with methanol and ammonia as working fluids, was observed and photographed by using a motion picture camera. with low pressure methanol, priming occurred easily with and without a thermal load applied. With the higher pressure ammonia, the artery could only be primed without a thermal load and the reliability of priming was poorer than with methanol. During the depriming process, the artery normally drained its fluid before the secondary wick desaturated. However, occasionally a complete dryout of the wick was observed before the artery deprimed. This is predicted by the hydrodynamic model. The results obtained from the analysis and from the tests with the glass heat pipe were applied to the OAO-C Level 5 heat pipe, and an improved correlation between predicted and measured evaporator and transport performance was obtained.

TABLE OF CONTENTS

1. INTRODUCTION

1.1 Background

Temperature control and thermal management of future large spacecraft will rely heavily on high performance heat pipes having high heat transport capability ($\int \dot{Q}\, dx$) and low ΔT. Of the many possible wick designs, the "composite wick" has the best potential of achieving these requirements. In composite wick heat pipes, the functions of capillary pumping and liquid transport are separated and can thus be independently optimized. The best known implementation of a composite wick is the arterial wick. Using ammonia as the working fluid, a heat transport capability of 920 watt-meters has been measured in a 1.27 cm diameter heat pipe (Ref. 1) and up to 3750 watt-meters in 2.5 cm diameter heat pipes (Ref. 2).

Unfortunately, the high performance of composite wick heat pipes is coupled with several disadvantages. The most troublesome disadvantage is that the composite wick must be primed before the high capability can be realized. An additional disadvantage is that the composite wick designs used in experimental heat pipes are difficult to manufacture and, therefore, do not lend themselves to quantity production. In spite of successful laboratory operation of several composite wick heat pipes, many aspects of their operation -- in particular, the priming and depriming process -- are not yet well understood. The purpose of the current program was, therefore, to provide a better understanding of these heat pipes and, thereby, to ultimately develop reliable space-flight hardware.

The most widely known composite wick heat pipes are those with an arterial wick. Typical arterial wicks are shown schematically in Figure 1.1. The "Pedestal Artery" (Figure 1.1.a) (Ref. 1) is being tested successfully on Level 5 of the OAO-C

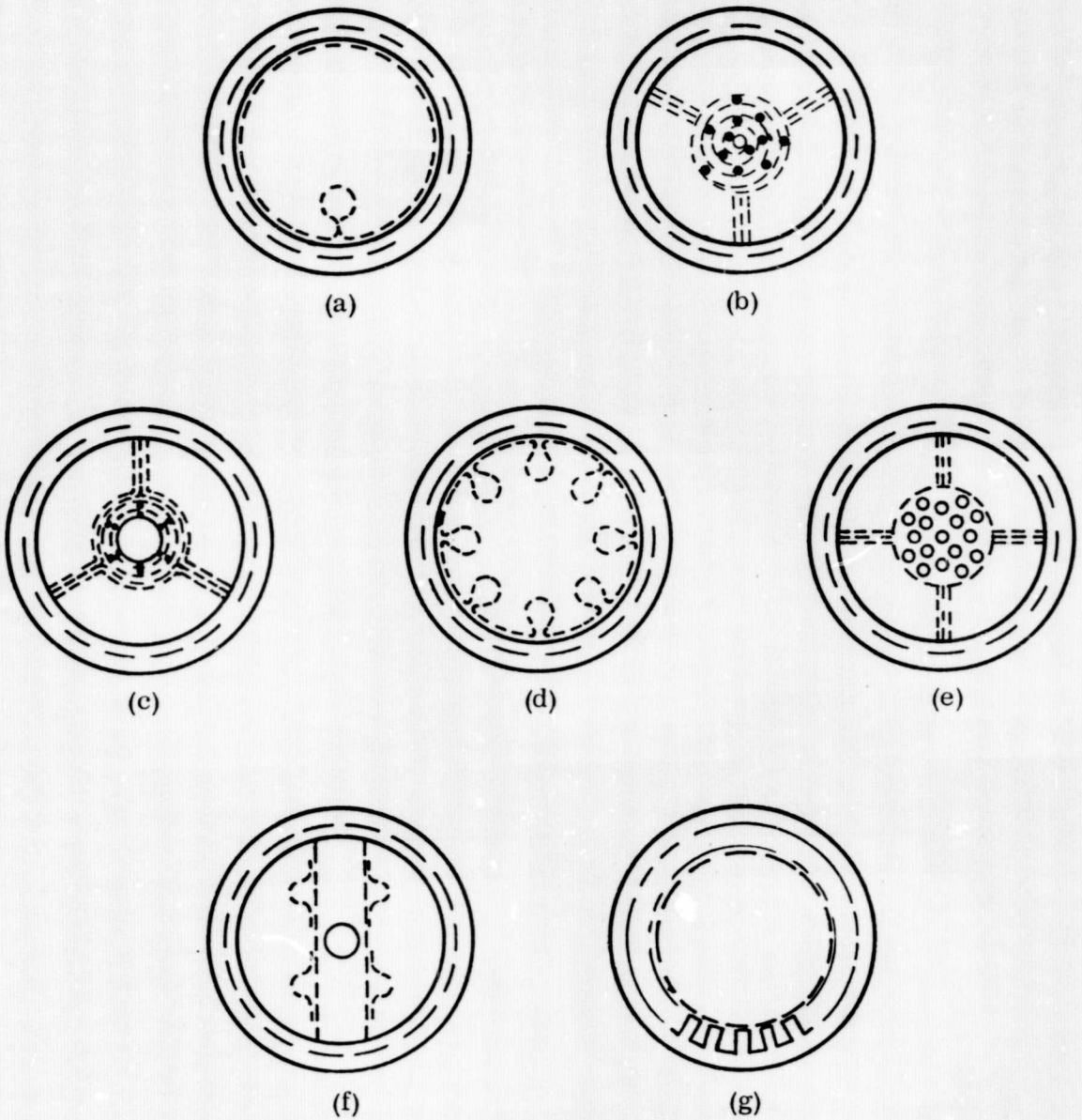

FIGURE 1.1

SCHEMATIC OF ARTERIES

spacecraft. The "Spiral Artery" (Figure 1.1.b) (Ref. 3) was also tested successfully aboard the same spacecraft. A variation of the spiral artery is the "Tunnel or Clapeyron Artery" (Figure 1.1.c) (Ref. 2). Concepts of heat pipes with multiple arteries are shown in Figures 1.1.d and 1.1.e (Ref. 4). A combination of arterial and porous screen wicks is employed in the design shown in Figure 1.1.f (Ref. 5). Finally, axial grooves covered with wire mesh represent another version of a multiple artery heat pipe (Ref. 6).

The common feature of all composite wicks is the relatively unobstructed liquid flow channels in combination with fine mesh porous material separating the liquid from the vapor. The liquid-vapor interface is located in the fine mesh porous material, and this provides high capillary pumping. The bulk of the liquid flows through the wider channels, and this provides the high permeability which results in low frictional pressure drop. The term "composite wick" applies to any wick in which the pores responsible for capillary pumping are of different size than the "pores" through which the bulk of the liquid flows. Thus, the arterial wick with its large flow passages is only a special case of the more general group of composite wicks. Other examples of composite wicks are the "Composite Slab" (Figure 1.2.a), the "Composite Circumferential Wick" (Figure 1.2.b), and the "Filled Artery" (Figure 1.2.c) (Ref. 7).

Most heat pipes employing a composite wick require a "secondary wick" for proper operation. If the main wick structure is located at or near the center of the heat pipe core, "bridges" or "pedestals" are usually employed to provide continuity for the liquid between the main wick and the heat pipe envelope (Figure 1.1.a through 1.1.e). Most designs also require a secondary wick for circumferential distribution of the liquid at the evaporator and condenser. Excluding screen covered grooves and the circumferential composite wick, all of the above designs employ a layer of screen or "screwthread

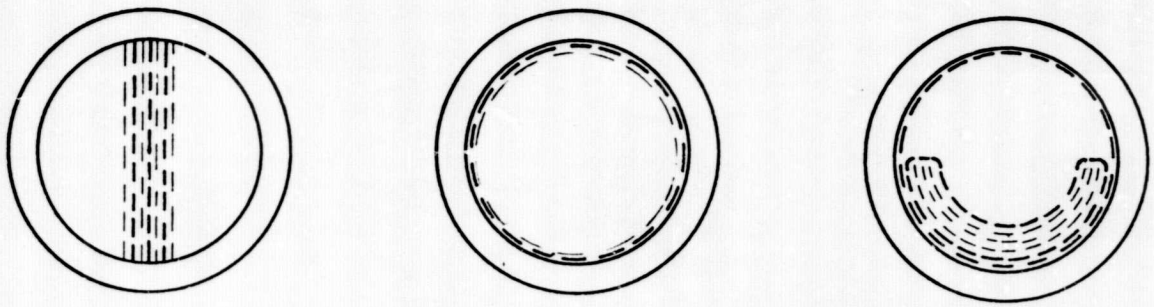

FIGURE 1.2

SCHEMATIC OF POROUS COMPOSITE WICKS

grooves" for circumferential distribution of the liquid. In order to fully understand the operational characteristics of a composite wick heat pipe, the effects of these secondary wicks must be considered along with the behavior of the main axial wick.

The obvious advantage of composite wicks is the combination of high capillary pumping and low liquid pressure drop resulting in very high axial heat transport capabilities. In order to realize the high capillary pumping capability of the small pore wick, the following two conditions must be met:

- The liquid-vapor interface must be located within the wick with the small pores.
- No vapor or gas bubbles which are larger than the pore size of the outer wick can exist within the coarse inner wick or the artery.

The first condition stipulates that the wick must be fully saturated; that is, sufficient working fluid must be present to fill the entire wick. The second condition is more difficult to achieve. Vapor bubbles may be generated within the artery as a result of nucleate boiling. Noncondensing gas bubbles may either be generated as a result of gas coming out of solution or may simply be trapped in the wick during the initial priming of the wick. Generally, the more open the flow passages of the coarser wick, the more sensitive the wick is to failures associated with vapor or gas bubbles.

Several mechanisms are available for priming the wick prior to start-up of the heat pipes. In a "zero g" environment, priming will occur automatically as a result of surface tension forces since the liquid will seek the state of lowest free energy which is attained when the wick is completely filled. In a "one g" environment, priming of the wick is usually accomplished as a result of surface tension forces, but the presence of

gravity opposes the filling of the wick since filling generally increases the potential energy of the system.

1.2 Objectives

Because of the relatively complex phenomena which occur in a composite wick heat pipe, the technology has not been sufficiently developed in order to make them work with high reliability. It was the purpose of this program to investigate, analytically and experimentally, several aspects of the composite wick with the ultimate goal being to develop reliable high-performance heat pipes for space applications. Specifically, two objectives were identified for this program:

(1) Analysis of Secondary Wick Effects

The primary wick serves the purpose of transporting the liquid phase of the working fluid in the axial direction from the condenser to the evaporator. The secondary wicks are responsible for radial and circumferential transport of the liquid from the condensing sites (usually at the wall of the heat pipe envelope) to the primary wick and, in the evaporator, from the primary wick to the evaporation sites. The secondary wick may severely reduce the overall heat transport capability of the heat pipe. The pressure losses in the secondary wick are porportional to the radial heat fluxes at the evaporator and condenser rather than the total axial heat flow rate. One of the objectives of this program was to generate an analytical model which includes the effects of the secondary wick on the axial heat transport capability.

(2) Development and Testing of a Glass Enveloped Arterial Wick Heat Pipe

While secondary wick effects reduce the heat pipe's transport capability

they usually do not cause complete failure. Insufficient priming, on the other hand, could cause a drastic reduction in the heat pipe's performance. Because of the complexity of the priming and depriming mechanisms, visual observation of these processes under actual operating conditions was desirable. An "inverted" glass heat pipe appeared to be the most versatile test vehicle to study the behavior of arterial heat pipes over a wide range of conditions. The second objective of the program was, therefore, to develop such a test vehicle and to study the priming and depriming processes of typical arterial wicks.

In keeping with the above objectives, a ten month development program was conducted by Dynatherm Corporation for GSFC. Because of the upcoming launch of the OAO-C spacecraft at the time of program initiation, the effort was concentrated on the pedestal artery heat pipe design since it was used in one of the OAO-C heat pipes. Many of the results, however, are applicable to other composite wick designs.

An analytical model was developed for the secondary wick effects in a pedestal type artery with screwthread circumferential grooves. The model describes the hydrodynamics of the circumferential flow with varying liquid cross-section in the absence of gravity. The normalized results are useful for use in determining the effect of evaporator heat flux on the axial heat transport capability for different groove designs. In general, a high density of small grooves is preferable at low evaporator heat fluxes while a low density of larger grooves is preferable at high fluxes.

During the experimental phase of the program, an "inverted" glass heat pipe was developed and tested. In an inverted heat pipe, the wick structure is attached to the outside of a metal tube and the heat source and sink are located inside. Tube and wick are placed inside a glass tube. With this arrangement, the liquid within the wick

can be directly observed while evaporation and condensation occurs radially as in a regular heat pipe. The inverted heat pipe was equipped with a pedestal artery and a single layer of screen for circumferential distribution. Priming and depriming mechanisms were observed with methanol and ammonia as working fluids. The general conclusions were that reliable priming can be achieved if the artery is initially dry; but, in a glazed artery, bubbles are usually entrapped. With methanol, which has a low vapor pressure at room temperature, priming occurred easily even with a thermal load applied. With high pressure ammonia, the artery could only be primed in the absence of any load and even then the reliability was not entirely satisfactory. Depriming of the artery, as a result of excessive heat load, normally occurs before the circumferential screen desaturates. However, occasionally a complete dryout of that screen was observed before the artery deprimed. Toward the end of the program, the single layer of screen was replaced with a screwthread as circumferential wick. The filling and drying of the grooves proved to be very difficult to observe and, therefore, no additional information was obtained.

The priming and depriming of the pedestal artery was photographed by GSFC personnel with regular speed and slow speed cameras. The film strips show the gradual collapse of a vapor bubble during priming and the extremely fast growth of a bubble during depriming.

The analytical results on the effects of evaporator heat flux on axial heat transport capability were tested with an OAO-C qualification heat pipe. It had been observed that the measured heat transport ($\dot{Q}L$) was in excess of that predicted by the screwthread model. The retesting of that pipe under controlled conditions showed that the grooves were dried out at high heat inputs and that circumferential heat transfer occurred only by conduction in the tube wall. Thus, the test results confirmed the analytical model in the

sense that the predicted heat transport capability was not exceeded; and the artery continued to operate even with dried-out grooves.

2. ANALYSIS

2.1 General Description of Model

The overall system performance is determined by the interaction of the primary and secondary wicks. Basically, the primary wick provides axial heat transport; whereas the secondary wick is used for circumferential distribution of the liquid in the evaporator and condenser sections. The common heat pipe hydrodynamic equations are applicable to both wick designs. An analysis has been conducted to determine the effect of the secondary wick on the heat pipe's performance. The following assumptions have been used:

- No gravitational forces are present.
- Heat is applied uniformly around the circumference of the tube at the evaporator and removed uniformly at the condenser.

A schematic of the model is shown in Figure 2.1. One or several arteries provide the axial flow passages for the liquid. At the evaporator and the condenser, the artery interfaces with a secondary wick which provides for circumferential distribution of the liquid. The artery and the secondary wick represent two flow resistances in series. Under load conditions, the hydrostatic pressure in the liquid decreases steadily from the condenser toward the evaporator and then continues to decrease within the secondary wick.

The pressure drop in the artery is proportional to the total axial heat flow rate $\dot{Q}$. The pressure drop in the secondary wick is proportional to the circumferential heat flow rate which is a function of $\dot{Q}$ and of the evaporator length. Since the two are independent of each other, no single value for the axial heat transport capability can be determined without specifying the evaporator length or, equivalently, the evaporator heat flux. The approach in this study is to determine the transport capability of primary and

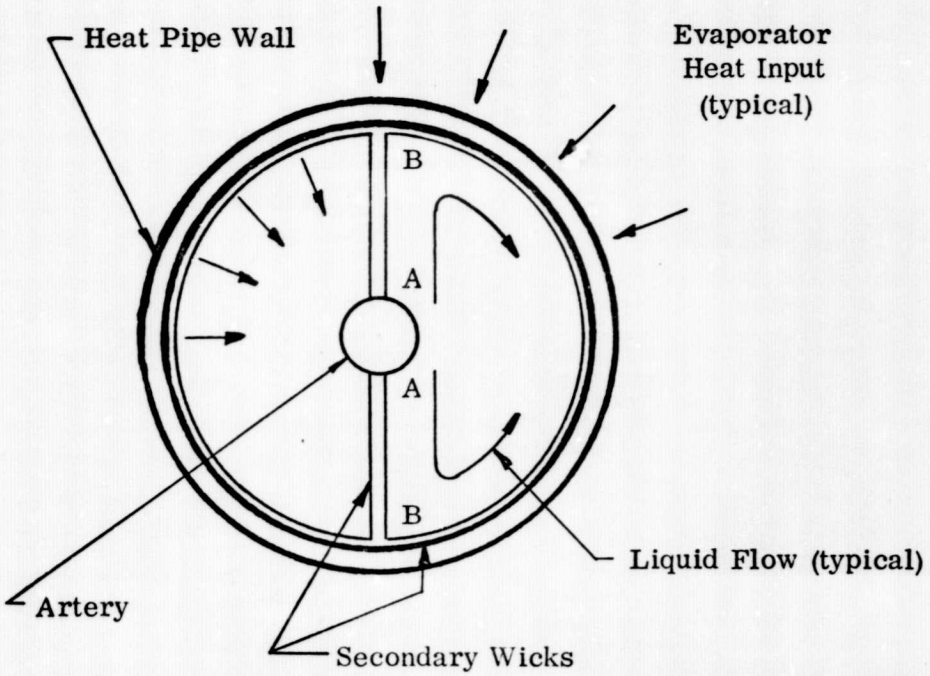

FIGURE 2.1

SCHEMATIC OF ARTERIAL HEAT PIPE
WITH BRIDGES AND SECONDARY WICK

secondary wicks independently and then to evaluate their interactions. Typically, the axial transport capability of the artery is severely degraded if the pressure drop in the secondary wick becomes appreciable.

Consistent with the pressure gradients in the liquid, the effective pumping radius of the meniscus will vary along the liquid flow paths. The effective pumping radius "r" is defined by:

$$\Delta p_i = \frac{2\sigma}{r} \qquad 2\text{-}1$$

where Δp_i is the interfacial pressure difference between liquid and vapor and σ is the surface tension of the liquid. In the absence of gravity, the maximum value of r anywhere in the heat pipe will be equal to the radius of the heat pipe envelope. The minimum value is given by the effective pore radius of each wick (Ref. 9). Thus, for the artery:

$$r_{a,p} < r_a < R \qquad 2\text{-}2$$

and for the secondary wick:

$$r_{s,p} < r_s < R \qquad 2\text{-}3$$

where

R = Radius of the heat pipe envelope

$r_{a,p}$ = Effective pore radius of the artery

$r_{s,p}$ = Effective pore radius of the secondary wick

The performance capability of each wick can be analyzed by applying the regular hydrodynamic equations to the artery and to the secondary wick separately. If the viscous pressure drop in the liquid is denoted as Δp_l, the pressure balance for artery and secondary wick can be written as:

$$2\sigma\left(\frac{1}{r_a} - \frac{1}{R}\right) = (\Delta p_l)\ \text{artery} \qquad 2\text{-}4$$

$$2\sigma\left(\frac{1}{r_{s,p}} - \frac{1}{r_s}\right) = (\Delta p_l)\ \text{secondary wick} \qquad 2\text{-}5$$

Continuity of pressure in the liquid requires that at the point of interface between arterial and secondary wick (Point A in Figure 2.1):

$$r_a = r_s \qquad 2\text{-}6$$

Δp_l of the artery is proportional to the axial heat flow rate $\dot{Q}$, and Δp_l of the secondary wick is proportional to the evaporator heat flux q_e. Thus, a simultaneous solution of Equations 2-4, 2-5, and 2-6 yields a relationship between the axial $\dot{Q}$ and the evaporator flux q_e.

In the above pressure balances the viscous or dynamic pressure losses in the vapor are not included. Since vapor losses are not of prime interest in this analysis, they will only be included in the summary equations.

Pressure drops in the liquid which occur in the condenser have also been omitted. This seems justified since most practical heat pipes contain a small amount of excess fluid which, in zero gravity, will form a slug at the condenser. This slug will have a meniscus with a radius of curvature equal to one-half the tube diameter. This slug then provides the "sump" from which the artery draws the liquid. Transfer of liquid from the film at the condenser to the slug could occur by shear forces from the vapor which would prevent the buildup of an excessive layer of liquid. Another driving force for transfer is the small capillary pressure difference between the slug ($\Delta p_i = \frac{2\sigma}{R}$) and the liquid in a film covering the condenser ($\Delta p_i = \frac{\sigma}{R}$). In the absence of a slug an analysis similar to the one for the evaporator would have to be conducted for the condenser.

In the following section, the hydrodynamics of the artery and of typical secondary wicks are considered separately. The effects of the secondary wick on the total axial transport capability is discussed in Section 2.3.

2.2 Hydrodynamics of Artery and Secondary Wicks

2.2.1 Artery

The axial pressure gradient in an artery of circular cross-section is given by Reference 9.

$$\frac{dp_l}{dx} = \frac{128 \mu_l \dot{Q}_a(x)}{\pi \lambda \rho_l D^4} \qquad 2\text{-}8$$

with

μ_l = Viscosity of the liquid

ρ_l = Density of the liquid

λ = Heat of evaporation

D = Diameter of artery

$\dot{Q}_a(x)$ = Local axial heat flow rate

Equation 2-8 can be integrated to yield the required capillary pressure difference between evaporator and condenser:

$$(\Delta p_l)_{artery} = \frac{128 \mu_l}{\pi \lambda \rho_l D^4} \int_o^L \dot{Q}_a \, dx \qquad 2\text{-}9$$

By introducing the effective transport length L_{eff}, the integral can be evaluated in terms of the total axial heat flow rate $\dot{Q}$:

$$\int_o^L \dot{Q}_a \, dx = \dot{Q} L_{eff} \qquad 2\text{-}10$$

Combining Equations 2-4, 2-9, and 2-10 yields for the hydrodynamic transport capability of the artery:

$$2\sigma\left(\frac{1}{r_a} - \frac{1}{R}\right) = \frac{128\,\mu_l}{\pi\,\lambda\,\rho_l\,D^4}\,\dot{Q}L_{eff} \qquad 2\text{-}11$$

The axial transport capability reaches a maximum when the effective pumping radius r_a, at the point of the interface with the secondary wick, becomes equal to its minimum value which is $r_{a,p}$. Thus:

$$(\dot{Q}L_{eff})_{max} = \frac{\pi D^4 N_l}{64\, r_{a,p}}\left(1 - \frac{r_{a,p}}{R}\right) \qquad 2\text{-}12$$

where

$$N_l = \text{Liquid Transport Factor} = \frac{\sigma\lambda\rho_l}{\mu_l}$$

The above maximum value can only be achieved if the pumping radius at the interface point can actually attain its minimum value $r_{a,p}$. Frequently, this is not consistent with the hydrodynamic requirements in the secondary wick.

2.2.2 Secondary Wick

The purpose of the secondary wick is to circumferentially distribute the liquid from the primary artery to the interior surface of the heat pipe. In most heat pipes, the secondary wick consists of two components:

- A circumferential wick which distributed the liquid over the evaporator surface.
- Bridges or pedestals which provide flow passages between the artery and the wall.

In the following sections, the hydrodynamics of these components are discussed separately.

2.2.3 Screen Circumferential Wick

Frequently, single or multilayer screens are used for circumferential distribution of the fluid from the artery to the evaporation sites.

The radial evaporator heat flux q_e is related to the total axial heat flow rate $\dot{Q}$ through:

$$q_e = \frac{\dot{Q}}{\pi D_o l_e} \qquad 2\text{-}13$$

where

D_o = Inner diameter of heat pipe

l_e = Length of evaporator

Referring to the symbolism of Figure 2-2, the circumferential mass flow rate is given by:

$$\dot{m}(y) = \frac{q_e l_e y_{max}}{\lambda}\left(1 - \frac{y}{y_{max}}\right) \qquad 2\text{-}14$$

The viscous pressure gradient in the circumferential screen wick can be expressed as:

$$\frac{dp_l}{dy} = -\frac{\mu_l y_{max} q_e}{K t l_e \rho_l} \qquad 2\text{-}15$$

where

K = Permeability of the screen wick

t = Thickness of the screen

Combining Equations 2-13, 2-14, and 2-15 gives:

$$\frac{dp_l}{dy} = \frac{\mu_l y_{max} q_e}{K t \rho_l \lambda}\left(1 - \frac{y}{y_{max}}\right) \qquad 2\text{-}16$$

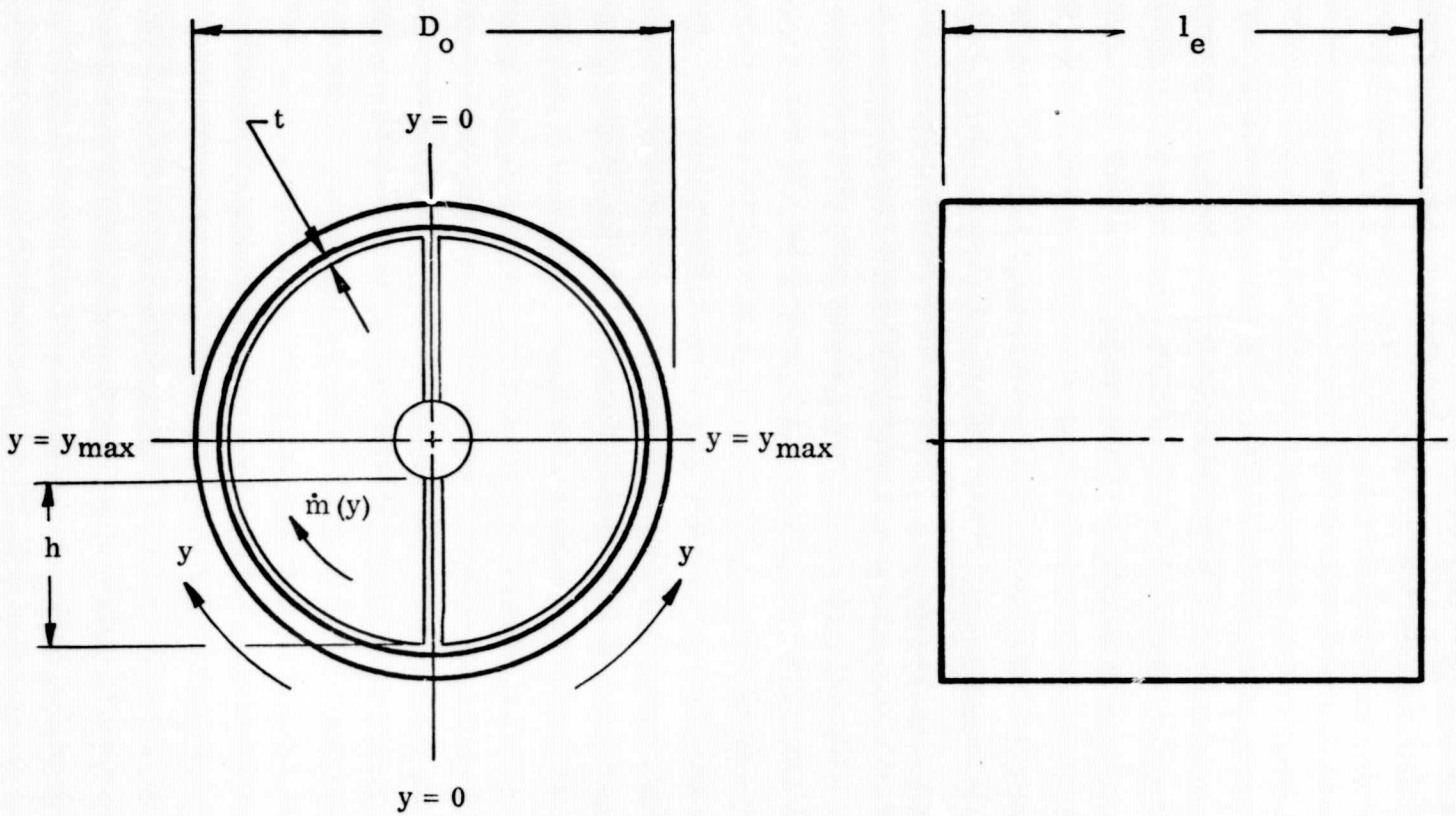

FIGURE 2.2

DEFINITION OF SYMBOLS FOR SECONDARY WICK MODEL

Equation 2-16 can be directly integrated to yield the pressure difference in the liquid which must be compensated for by capillary forces:

$$(\Delta p_l)_{screen} = \frac{\mu_l q_e y_{max}^2}{2 K t \rho_l \lambda} \qquad 2\text{-}17$$

After substituting the corresponding pumping radii (Equation 2-5), the maximum permissible evaporator heat flux can be expressed as:

$$q_e = \frac{4 K t \rho_l \lambda \sigma}{\mu_l y_{max}^2} \left(\frac{1}{r_{s,p}} - \frac{1}{r_o} \right) \qquad 2\text{-}18$$

Equation 2-18 gives the evaporator heat flux as a function of the pumping radius r_o at the "injection point" (Point B in Figure 2.1). If this heat flux is exceeded the circumferential screen wick would dry out beginning at the point $y = y_{max}$.

The upper limit for the radius at the injection point is $r_o = R$. The corresponding limiting evaporator heat flux is:

$$(q_e)_{max} = \frac{4 K t \rho_l \lambda \sigma}{\mu_l y_{max}^2 r_{s,p}} \left(1 - \frac{r_{s,p}}{R} \right) \qquad 2\text{-}19$$

But this heat flux can be reached only if the axial heat load approaches zero. Conversely, in order for the heat pipe to pump axially and circumferentially, the operating heat flux at the evaporator must be less than the maximum value. This relationship is more fully discussed in Section 2.3.

2.2.4 Screwthread Grooves as Circumferential Wick

Fine screwthread grooves which are machined into the heat pipe wall provide a very effective circumferential wick. The hydrodynamic analysis of the grooves is similar to that of the circumferential screen wick but with the additional complication that the liquid

rlow area and thus the permeability vary along the azimuthal flow path.

The azimuthal pressure gradient within each groove is given by the same type of equation as for the screen wick:

$$\frac{dp_l}{dy} = - \frac{\mu_l \dot{m}(y)}{K(y)\, A_l(y)\, \rho_l} \qquad 2\text{-}20$$

where $\dot{m}(y)$ now represents the mass flow rate within a single groove.

In Equation 2-10, both the permeability K and the liquid cross-sectional area of each groove vary with the azimuthal coordinate y. Next, the analytical expressions for these two parameters are developed and then integrate Equation 2-20. Unfortunately, the analytical expressions are different for completely and partially filled grooves.

First, consider the partially filled groove shown in Figure 2-3. In order to keep the solution general it is assumed that the threads are not fully developed; i..e, a "land" exists between adjacent grooves.

It is convenient to express the permeability and the liquid area in terms of the radius of curvature of the meniscus. From Figure 2-3:

$$\cos\alpha = \frac{S(y)}{r(y)} \qquad 2\text{-}21$$

where S(y) is the "wetted" groove width. The liquid cross-sectional area is equal to the triangular area based on the wetted groove width less the void segment inscribed by the radius of curvature.

$$A_l(y) = r^2(y) \left[\frac{\cos^2\alpha}{\tan\alpha} - \frac{1}{2} (\pi - 2\alpha - \sin 2\alpha) \right] \qquad 2\text{-}22$$

The above equation only applies strictly to a groove with a sharp point at its bottom. If the radius at the bottom of the groove is finite, the actual area will be slightly smaller

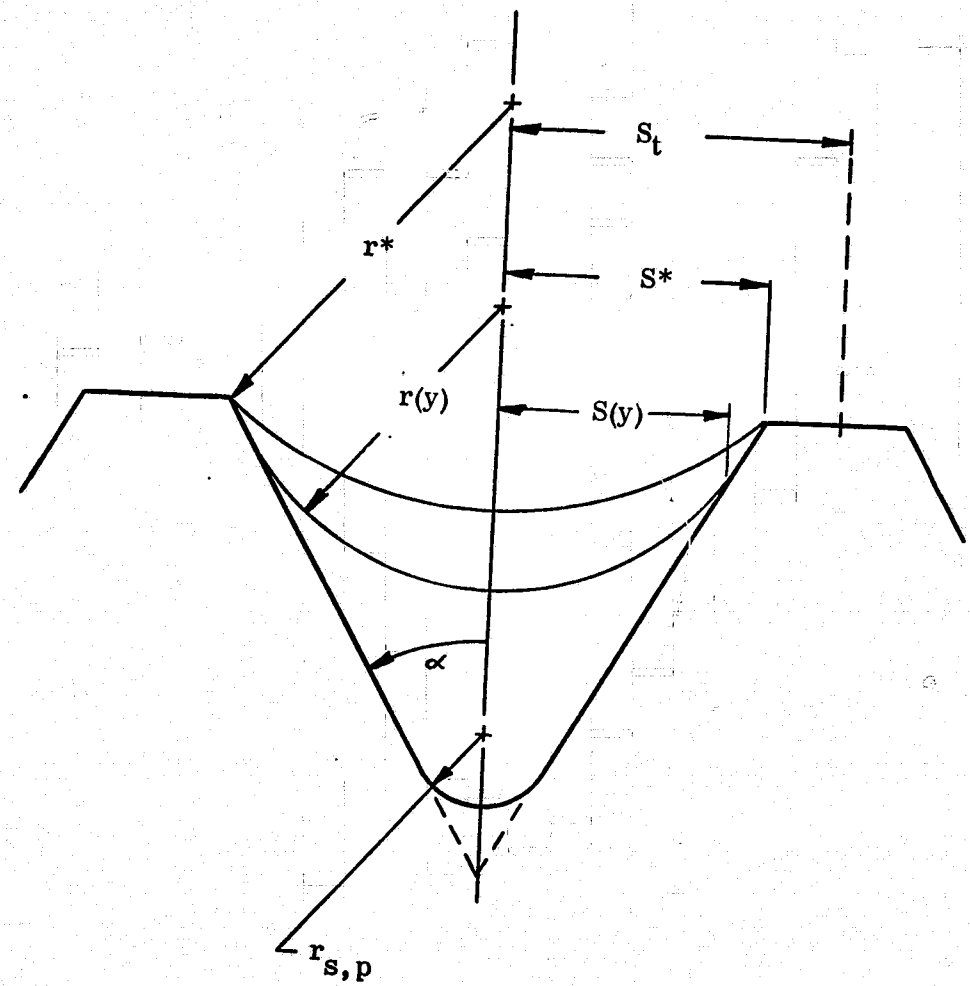

FIGURE 2.3

SCHEMATIC OF CIRCUMFERENTIAL GROOVE

than given by Equation 2-22.

The effective permeability K is related to the hydraulic diameter D_h through:

$$K = \frac{D_h^2}{32} \qquad 2\text{-}23$$

And the hydraulic diameter is based on the relationship:

$$D_h(y) = \frac{4\,A_l(y)}{P(y)} \qquad 2\text{-}24$$

where P(y) is equal to the wetted perimeter of the triangular groove. The corresponding expression, when the proper terms are substituted in Equation 2-24, is:

$$D_h(y) = r(y)\left[2\cos^2\alpha - \tan\alpha\,(\pi - 2\alpha - \sin 2\alpha)\right] \qquad 2\text{-}25$$

Substitution of Equations 2-22, 2-23, and 2-25 into Equation 2-20 gives the azimuthal pressure gradient in a triangular groove as a function of the radius of curvature of the meniscus.

A somewhat more complicated expression can be derived for the liquid cross-sectional area and the permeability, if the radius of the meniscus exceeds a critical value r*. In reference to Figure 2.3, this critical r* is given by:

$$\cos\alpha = \frac{S^*}{r^*} \qquad 2\text{-}26$$

where S* is the geometrical width of the groove. In this second case, the wetted groove always equals the maximum groove width and the radius of the meniscus varies between r* and R (the upper limit being the heat pipe radius).

The proper arithmetic leads to the following approximate expressions for the liquid area and the hydraulic diameter for this fill condition:

$$A_l(y) = r^2(y)\,\phi^2\left[\frac{\cos^2\alpha}{\tan\alpha} - \frac{1}{2}\left\{(\phi\cos\alpha) + \frac{1}{2}(\phi\cos\alpha)^3 + \frac{1}{12}(\phi\cos\alpha)^5\right\}\right] \qquad 2\text{-}27$$

$$D_h(y) = r(y)\,\phi\left[2\cos\alpha - \tan\alpha\left\{(\phi\cos\alpha) + \frac{1}{2}(\phi\cos\alpha)^3 + \frac{1}{12}(\phi\cos\alpha)^5\right\}\right] \quad 2\text{-}28$$

The parameter ϕ in the preceding equations is defined as:

$$\phi = \frac{r^*}{r(y)} \quad 2\text{-}29$$

By substituting Equations 2-22 and 2-23 or 2-27 and 2-28 into 2-20 the pressure gradient in the liquid is obtained.

The objective of this analysis is to express the maximum heat flux q_e in terms of the effective pumping radius at the injection point. This can be done by integrating the pressure gradient along the groove. In order to do so, an additional equation relating the pressure gradient to the azimuthal change in the radius of the meniscus is required. This equation can be found from the definition of the interfacial pressure difference due to capillary forces:

$$\Delta p_i = \frac{2}{2\,r} = \frac{\sigma}{r} \quad 2\text{-}30$$

(Note that in a groove the effective pumping radius is twice the geometrical radius of the meniscus.) Differentiating Equation 2-30 yields:

$$\frac{d(\Delta p_i)}{dx} = -\frac{\sigma}{r^2(y)}\frac{dr}{dy} \quad 2\text{-}31$$

Equilibrium of forces requires:

$$\frac{dp_l}{dy} = -\frac{d(\Delta p_i)}{dy} \quad 2\text{-}32$$

Substituting Equations 2-20 and 2-31 into 2-32 yields for each individual groove:

$$-\frac{\mu_l\,\dot{m}(y)}{K(y)\,A_l(y)\,\rho_l} = \frac{\sigma}{r^2(y)}\frac{dr(y)}{dy} \quad 2\text{-}33$$

For uniform evaporator heat flux the mass flow rate in a single groove is related to the evaporator heat flux as follows:

$$\dot{m}(y) = \frac{2 q_e S_t y_{max}}{\lambda} \left(1 - \frac{y}{y_{max}}\right) \qquad 2\text{-}3$$

By substituting the appropriate terms into Equation 2-33 and integrating it, an equation expressing the radius of the meniscus as a function of the azimuthal coordinate y can be obtained:

$$r(y) = \frac{1}{\cos\alpha} \left[\cos^3\alpha \; r(0) - \frac{3}{2} \psi S_t y (2 y_{max} - y)\right]^{1/3} \qquad 2\text{-}3$$

where $r(0)$ = radius of meniscus at the injection point and the parameter ψ is defined as:

$$\psi = \frac{16 q_e \mu_l}{\sigma \lambda \rho_l} \left\{ \frac{8 \sin^3\alpha}{\tan^2\alpha \left[2 \cos^2\alpha - \tan\alpha (\pi - 2\alpha - \sin 2\alpha)\right]^3} \right\} \qquad 2\text{-}3$$

For a fixed radius of curvature at the injection point $r(0)$, the permissible evaporator heat flux reaches a maximum if the radius of the meniscus approaches $r_{s,p}$ at $y = y_{max}$. In order to simplify the general analysis $r_{s,p}$ is assumed to be equal to zero, corresponding to a groove with a sharp point at its bottom. (During numerical analysis and data correlation, this simplification was not exercised but the true measured $r_{s,p}$ was used.) Applying the boundary condition $r(y_{max}) = 0$, the expression for q_e can be derived as a function of the radius of curvature at the injection point:

$$q_e = \frac{\beta N_l r^3(0) \cos^3\alpha}{24 S_t y_{max}^2} \qquad 2\text{-}3$$

where

N_l = Liquid Transport Factor

$$\beta = \frac{1}{8} \frac{\tan^2 \alpha}{\sin^3 \alpha} \left[2 \cos^2 \alpha - \tan \alpha (\pi - 2\alpha - \sin 2\alpha) \right]^3 \qquad 2\text{-}38$$

(For a standard 60^o thread, β is equal to 0.164.)

For the case where the radius of the meniscus at the injection point exceeds the critical radius r*, the pressure gradient (Equation 2-20) must be integrated in two steps:

- For $0 < y < y^*$, Equations 2-22 and 2-25 apply for the liquid flow area and the hydraulic diameter, respectively. The critical azimuthal location y* is herein defined by the equation:

$$r(y^*) = r^* \qquad 2\text{-}39$$

- For $y^* < y < y_{max}$, the liquid flow area and the hydraulic diameter are given by Equations 2-27 and 2-28.

After integration over both regions and applying the appropriate boundary conditions, namely:

$$\begin{array}{lll} r = r(0) & \text{at} & y = y_o \\ r = r^* & \text{at} & y = y^* \\ r = 0 & \text{at} & y = y_{max} \end{array} \qquad 2\text{-}40$$

an equation for q_e which is equivalent to Equation 2-37 can be formulated:

$$q_e = \frac{\zeta N_1 r^{*3} \cos^3 \alpha}{24 S_t y_{max}^2} = \frac{\zeta N_1 S^{*3}}{24 S_t y_{max}^2} \qquad 2\text{-}41$$

where,

$$\zeta = \frac{1}{2} \left[\beta + 0.75 \delta \cos \alpha + \sqrt{\beta^2 + 1.5 \delta \beta \cos \alpha} \right] \qquad 2\text{-}42$$

The parameter δ is a function of the ratio $\phi_o = r^*/r(0)$ which ranges from $\phi_o = 1$ to

$\phi_o = r^*/R$. For a standard thread of 60^o, δ can be approximated by the following equation:

$$\delta = 2.78 + \phi_o \left[0.12\, \phi_o^{3.72} - \phi_o^{2.48} + 3.29\, \phi_o^{1.24} - 5.19 \right] \qquad 2\text{-}43$$

The above set of equations express the maximum permissible evaporator heat flux for a given groove geometry as a function of the radius at the injection point. If that radius is less than the critical radius r* (see Figure 2-3), the applicable equation is 2-37. If that radius exceeds r*, the approximation 2-41 applies. Both equations are strictly valid only if the bottom of the triangular groove consists of a sharp point ($r_{s,p} = 0$). They are equivalent to the corresponding Equation 2-18 for the screen secondary wick.

2.2.5 Pedestal and Bridges

In many heat pipe designs, the artery (or arteries) do not interface directly with the secondary wick but are separated from the latter by pedestals or bridges. The pressure drop through these bridges must be added to the pressure drop in arteries and secondary wick. It is given by:

$$(\Delta p_l)_{bridge} = \frac{\mu_l \pi D_o h q_e}{\rho_l \lambda N t_b K_b} \qquad 2\text{-}44$$

where

N = Number of bridges

t_b = Thickness of the screen forming the bridges

K_b = Permeability of the bridge material

h = Height of pedestals or length of bridge

Associated with this pressure drop is a decrease of the effective meniscus along the bridge between the artery and the injection point of the secondary wick. Thus, whenever

a bridge is employed, the pumping radius r_o at the injection point for the circumferential wick differs from the radius r_a at the interface between artery and secondary wick in accordance with the following equation:

$$2\sigma\left(\frac{1}{r_o} - \frac{1}{r_a}\right) = \frac{\mu_l \pi D_o h q_e}{\rho_l \lambda N t_b K_b} \qquad 2\text{-}45$$

2.3 Effects of Secondary Wick on Axial Transport Capability

For an arterial heat pipe which utilizes a secondary wick, the minimum value of r_a in Equation 2-11 is dictated by the evaporator heat flux. If no bridges are used, r_a must equal r_o in Equations 2-18, 2-37, or 2-41. If bridges are used r_a and r_o are related through 2-45. The resulting heat transport limitation can be determined as a function of the evaporator heat flux by simultaneous solution of the above equations.

These relationships can be generalized by expressing the results in dimensionless terms such as the axial heat transport ratio and the normalized eavporator heat flux. The first ratio is defined as the actual heat transport capability for a particular normalized evaporator flux as compared to the maximum heat transport capability of the primary wick. For very low heat fluxes, this ratio is equal to its maximum value of 1.0. The normalized evaporator heat flux φ is defined as:

$$\varphi = \frac{q_e}{N_l} \qquad 2\text{-}46$$

where N_l is again the Liquid Transport Factor of the working fluid which also has the dimension of a heat flux.

The heat transport ratio is equal to the ratio of Equations 2-11 and 2-12 and may be written as:

$$\frac{\dot{Q}L}{(\dot{Q}L)_{max}} = \frac{r_{a,p}}{r_a} \frac{1 - \frac{r_a}{R}}{1 - \frac{r_{a,p}}{R}} \qquad 2\text{-}47$$

This ratio is only a function of r_a, the capillary radius at the interface point with the secondary wick. When bridges or pedestals are employed, r_a is related to Equation 2-45. r_o is the radius at the injection point for the circumferential wick. Equation 2-45 can be written in the following form:

$$\frac{1}{r_o} - \frac{1}{r_a} = \frac{\pi D_o q_e h}{2 N t_b K_b N_l} \qquad 2\text{-}48$$

In the absence of bridges $r_a = r_o$. Expressions for r_o were derived in previous sections as a function of the evaporator heat flux for both the screen and the groove secondary wick.

The equations have been programmed for a computer solution. This program has been utilized to generate performance curves for heat pipes having a diameter of 1.27 cm, a single artery with one pedestal, and with groove spacings ranging from 12.5 to 28 grooves per centimeter.

Typical results are presented graphically. Figure 2.4 gives the maximum radial heat flux (normalized by the Liquid Transport Factor) for fully threaded grooves (standard 60^o thread). A fully threaded groove design exists when the groove width S* is equal to the pitch of the thread S_t. As the number of threads per unit length decreases, the grooves become deeper and thus more liquid flow area is available. This results in a higher maximum heat flux capability.

The effect of a partial thread is shown in Figure 2.5. The solid curve represents the degradation of the maximum evaporator heat flux when the ratio S^*/S_t is less than unity.

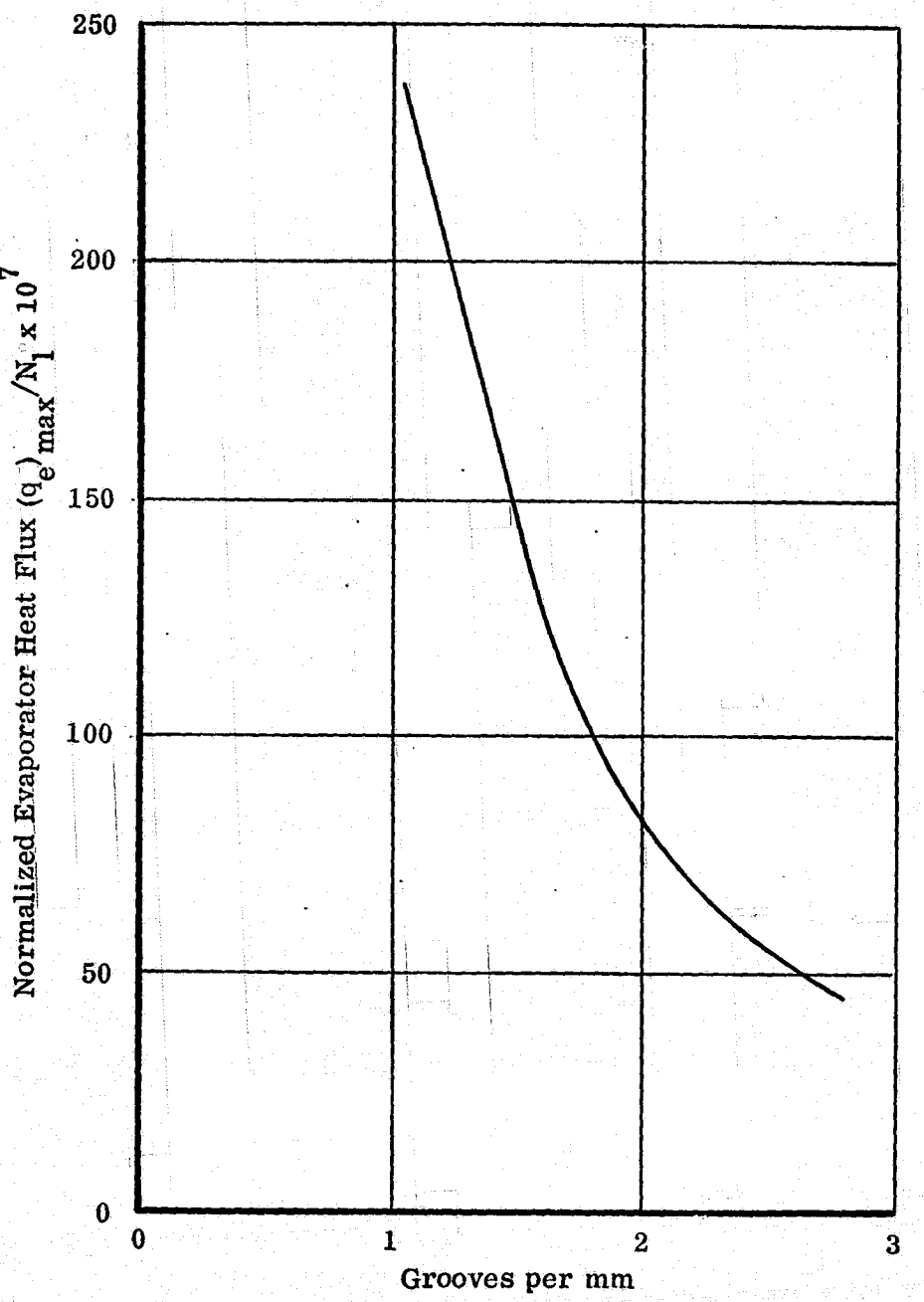

FIGURE 2.4

NORMALIZED MAXIMUM HEAT FLUX OF
CIRCUMFERENTIAL GROOVES VS.
NUMBER OF GROOVES PER MM

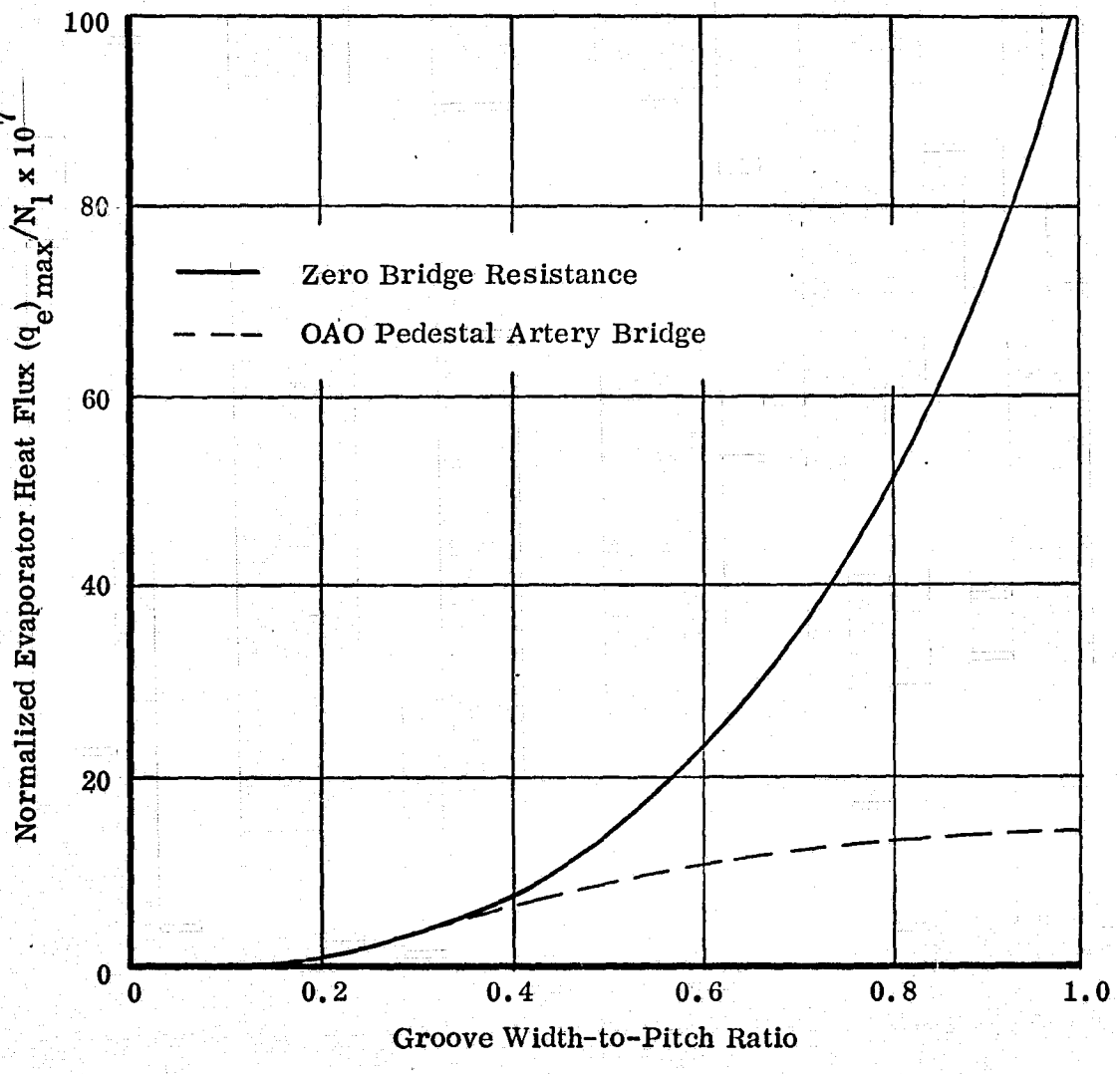

FIGURE 2.5

NORMALIZED EVAPORATOR HEAT FLUX OF
CIRCUMFERENTIAL GROOVES FOR
PARTIAL GROOVE DESIGN
(2 grooves per mm)

The solid curve shows the same effect but in the presence of a bridge resistance which is typical of the OAO-C heat pipe pedestal.

Figure 2.6 shows the heat transport ratio $(\dot{Q}L)/(\dot{Q}L)_{max}$ as a function of the normalized evaporator heat flux for several thread densities (pitches). Two important conclusions can be drawn from this figure:

- If the evaporator heat flux stays below a certain threshold value, the axial heat transport ratio is equal to unity, which means that the secondary wick does not degrade the performance of the artery. In this regime of heat fluxes the pumping radius at the injection point is less than the effective pore radius of the artery, thus the artery can develop its full capability
- At moderate evaporator heat fluxes a high thread density is advantageous, although the benefit is relatively small. At very high evaporator heat fluxes the opposite is true -- less degradation occurs if fewer threads are employed. However, the crossover occurs at a point where the axial heat transport capability is already severely degraded.

Finally, the effect of a partial thread is shown in more detail in Figure 2.7. At low evaporator heat fluxes, the axial transport capability is not affected by the thread design. At high heat fluxes, the transport capability is severely restricted if a partial thread is employed. However, for any practical thread design (e.g., $S^*/S_t > 0.2$), the degrading effect becomes serious only at heat fluxes where even a full thread degrades the axial transport capability to a point ($\leq 50\%$) that this no longer represents a desirable operating condition. In conclusion, the thread design is only of minor importance

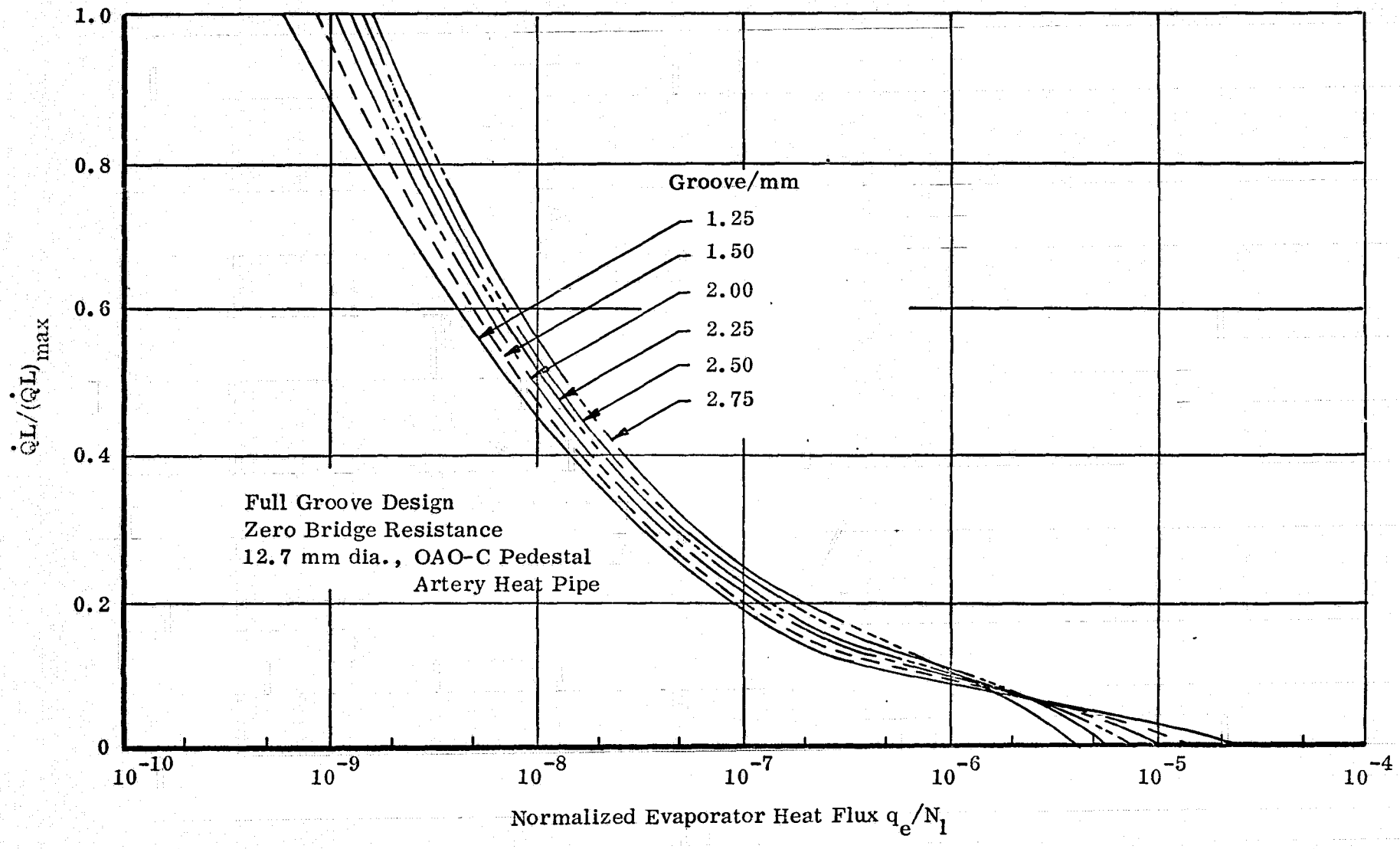

FIGURE 2.6

DIMENSIONLESS HEAT PIPE PERFORMANCE VS.
NORMALIZED EVAPORATOR HEAT FLUX

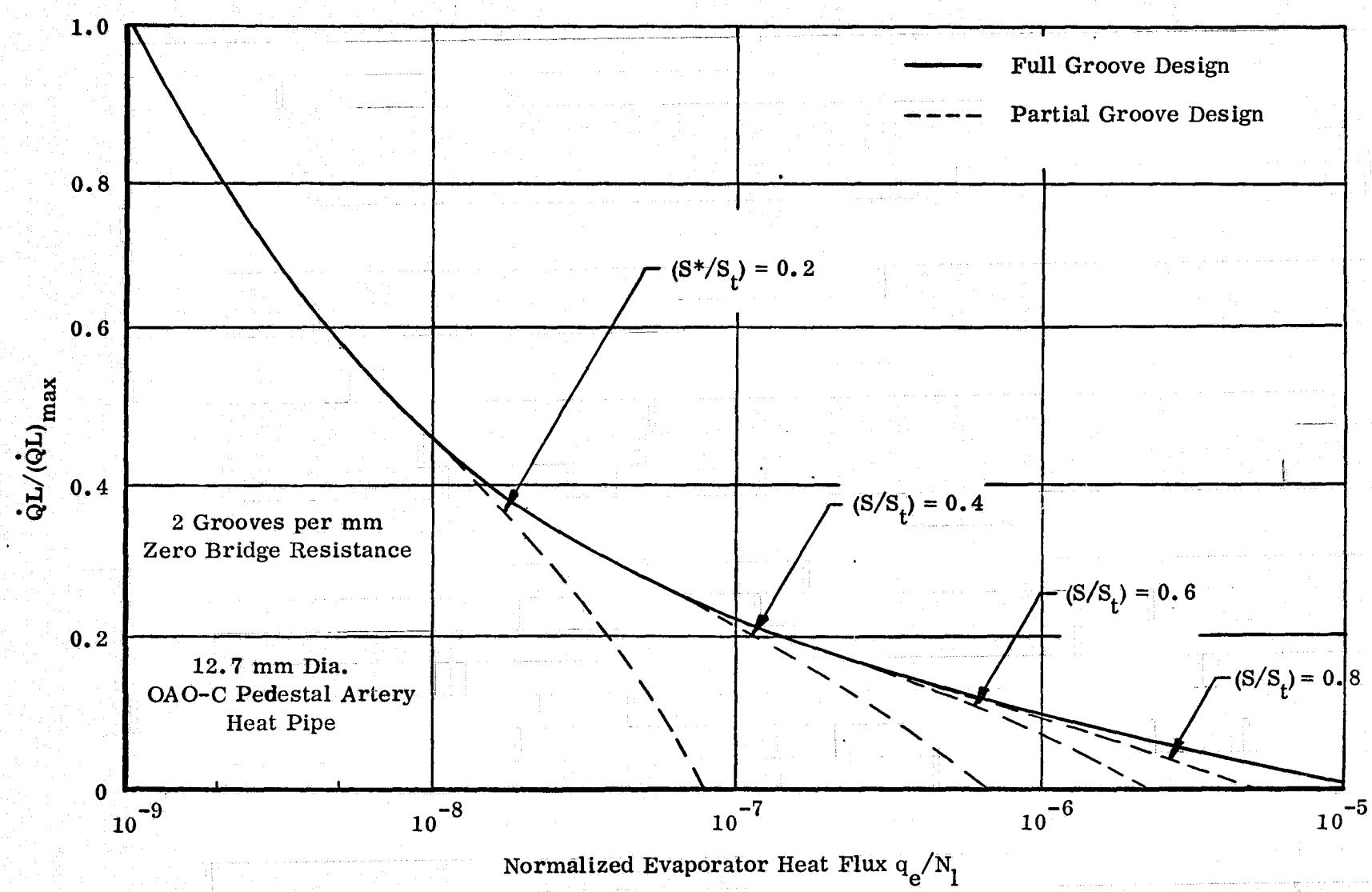

FIGURE 2.7

DIMENSIONLESS HEAT PIPE PERFORMANCE VS.
NORMALIZED EVAPORATOR HEAT FLUX

to the heat transport capability of the artery. The limitations imposed by the secondary wick can be more effectively overcome by using multiple injection points. However, the transport analysis does not consider the evaporation film coefficient associated with different secondary wick designs. In practical heat pipes, the evaporator film coefficient may be the dominating consideration in the selection of a particular secondary wick.

3. TEST PROGRAM

3.1 Test Vehicle

Very high heat transport capabilities have been observed with arterial heat pipes. For example, heat throughputs of 10,000 Watt-inches were achieved with an adverse gravity head of 7.0 cm. However, the start-up behavior has been erratic and an unpredicted drop-off in performance at low temperatures ($-40^{\circ}C$) has been observed. In view of these results and observations, a versatile test vehicle was designed which permitted more fundamental investigations of these phenomena. The design goals for this test vehicle were:

- Visual observation of the priming status of the arterial and secondary wick.
- Smallest possible perturbation of heat pipe operation by the requirement for observation.

The test vehicle is shown in Figure 3.1. It can be described as an "inverted" heat pipe which permits visual observation of all processes without the usual limitations of conventional glass heat pipes. A central metal tube contains a heater for the evaporator section, coolant passages at the condenser, and all instrumentation. The wick is located at the outside of the central tube as shown in the cross-sectional view of Figure 3.1. The working fluid is contained in the outer glass envelope. The evaporation and condensation processes occur through interfaces which are identical to those of a "real" heat pipe. Because of the glass envelope, all sections of the wick can be directly observed and all phases of operation monitored.

In order to provide for safe operation with ammonia the inverted heat pipe was placed inside a metal shield which was equipped with a viewing port. The entire test

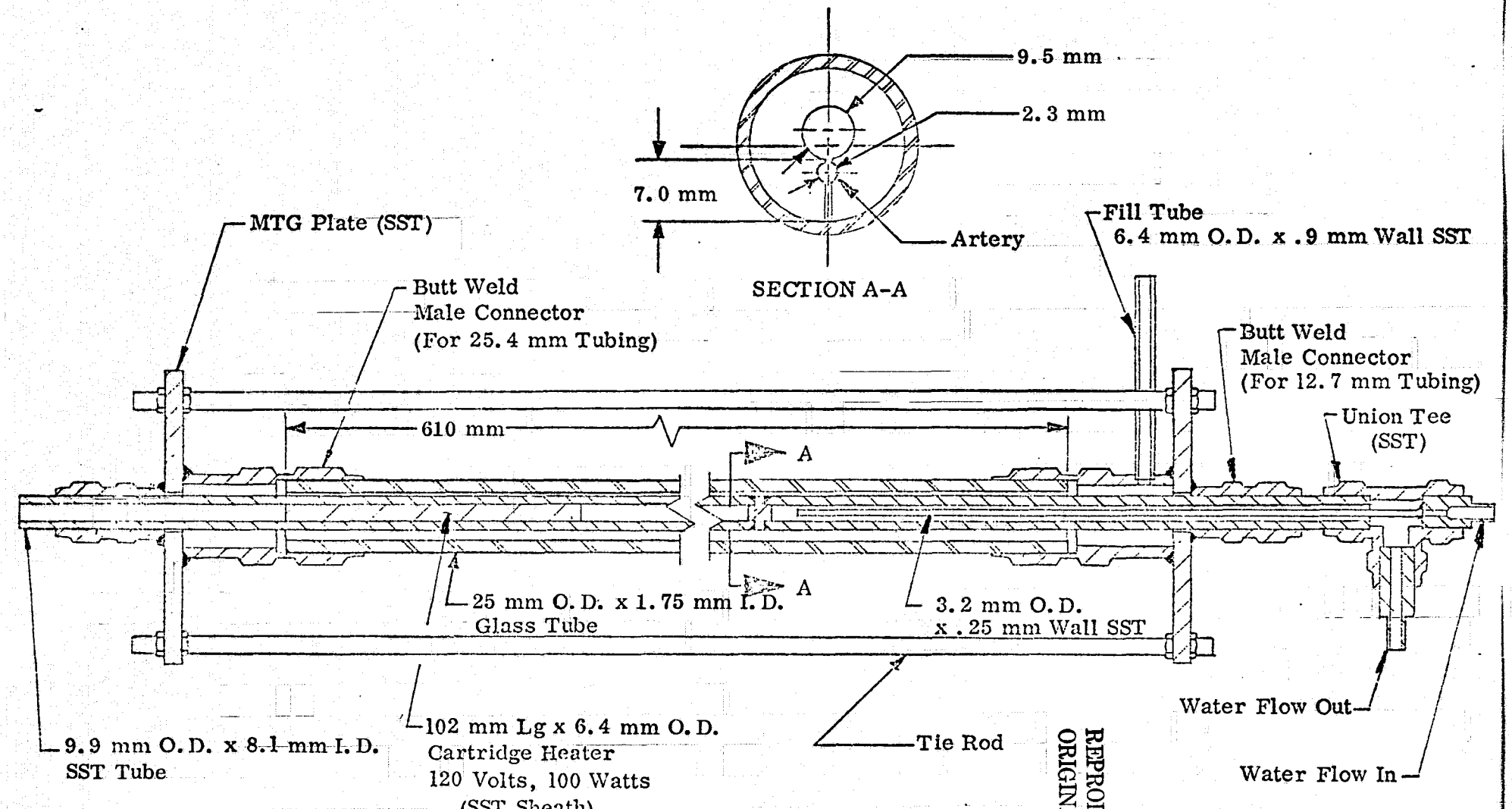

FIGURE 3.1

HEAT PIPE TEST VEHICLE

setup is shown schematically in Figure 3.2. The fluid reservoir which is located near the condenser end of the heat pipe is connected to the latter by thin, 3 mm diameter, stainless steel tubing. Adjustment of the fluid level within the heat pipe was made by raising or lowering of the reservoir. The mounting structure permitted adjustment of the orientation by ± 15 cm with respect to horizontal. Since feedthroughs for the thermocouples into the working space of the heat pipe seemed undesirable, all instrumentation was located inside the inner metal tube which was not part of the pressure vessel. At the specified location for each thermocouple a small hole was drilled into the metal tube, the thermocouple bead was fed from the inside through the hole and the bead, then TIG welded to the tube. In this manner a leak-tight closure was achieved and, at the same time, the bead of the thermocouple was located directly at the evaporating or condensing surface (Figure 3.3).

The primary wick for all tests consisted of a pedestal artery. It was formed of a single layer of 200-mesh screen with an inside diameter of 2.4 mm and attached by spot-welding to the bottom of the inner core tube. Lighting, by means of a fluorescent tube from behind, was arranged such that the liquid inside the artery could be observed everywhere in the artery. The bulk of the tests were conducted with a secondary wick consisting of a single layer of 200-mesh screen spotwelded around the inner core tube. Toward the end of the program the secondary screen wick was replaced by screwthread grooves on the core tube. Thirty-eight grooves per linear centimeter having an average depth of 0.19 mm and an average width of 0.28 mm were used.

3.2 Test Results and Data Correlation

3.2.1 Methanol Working Fluid - Single Layer Screen Secondary Wick

The majority of tests were conducted with this wick configuration and working

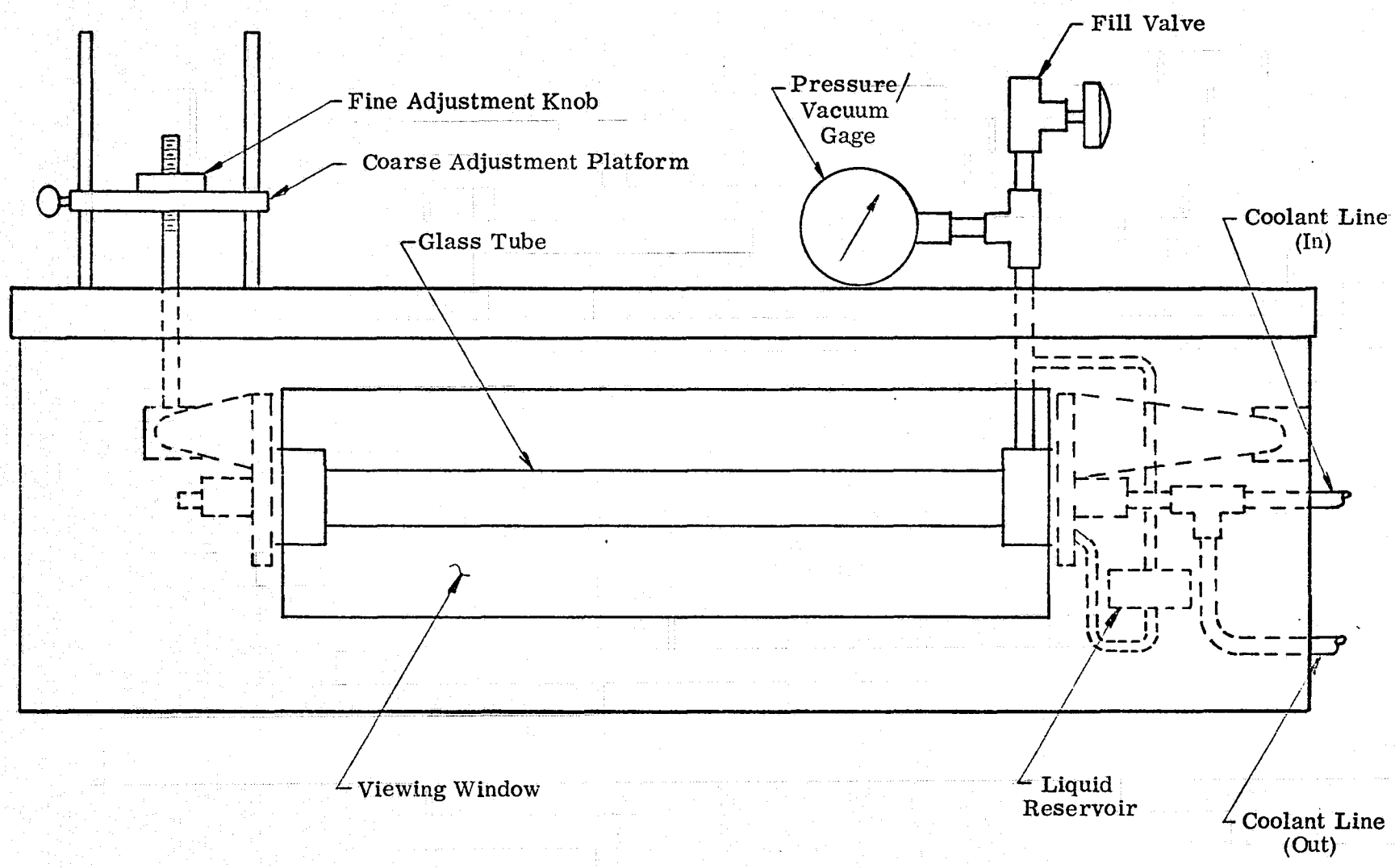

FIGURE 3.2

"INVERTED" HEAT PIPE TEST SYSTEM

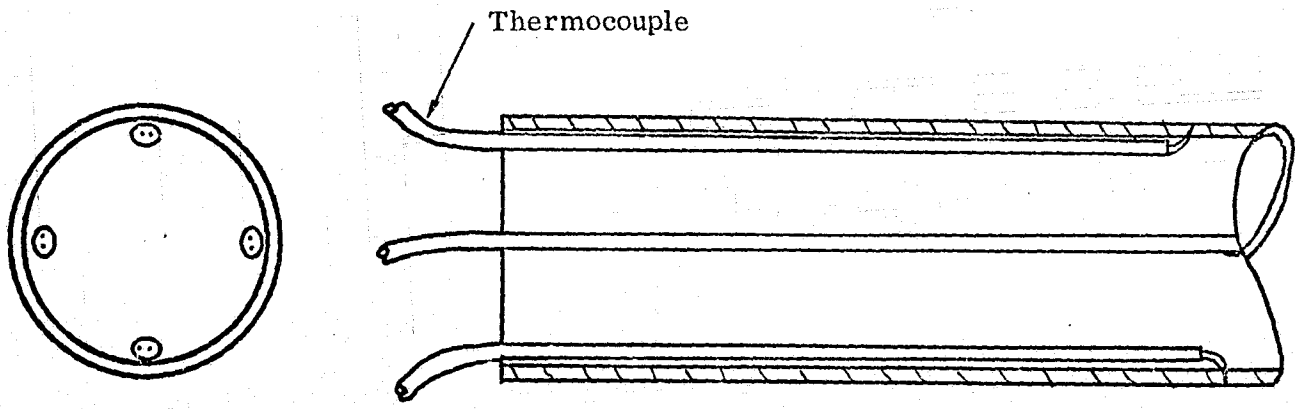

FIGURE 3.3

THERMOCOUPLE INSTALLATION IN INVERTED HEAT PIPE

fluid. Because the inverted heat pipe afforded the unique feature of direct observation of the artery priming and depriming, the emphasis during testing was on these phenomena; while the quantitative performance was only of secondary importance.

Two procedures to prime the artery were studied. The first approach was to prime when the artery was empty and when the 200-mesh wall of the artery was completely wetted. Repriming of this completely wetted (glazed) artery was not accomplished. The priming attempts were made with and without power applied. With no power, a vapor slug remained which was approximately 2 cm long. With power applied to the evaporator, the vapor slug flowed to the hot end and then grew in length.

The second method of priming was very successful. This procedure consisted of drying out the artery walls at the evaporator before initiating priming. After artery (and secondary wick) dryout occurred, the tilt of the heat pipe was adjusted such that the evaporator was elevated approximately 2.5 mm to 5 mm. At this position, the secondary wick (200-mesh screen against the heat pipe wall) can slowly and completely wet while the single layer screen walls of the artery cannot. As soon as this wetting was accomplished, the heat pipe evaporator was gradually lowered to the horizontal position to complete the priming of the artery. This procedure led to repriming in less than 5 minutes. Successful repriming by this method was accomplished repeatedly with and without power (up to 35 watts) applied to the evaporator. In a "zero g" environment, of course, no equivalent exists to this manipulation of the evaporator elevation. However, capillary forces will replace gravity for gradually filling the artery without at first wetting the single layer screen. This mechanism has been suggested before, and the above tests provided a visual and quantitative verification.

An extensive series of tests were conducted to study the burnout characteristics

of the arterial wick. The available instrumentation on a conventional, metal enclosed heat pipe does not permit a distinction between drying out of the secondary wick (e.g., circumferential screen or grooves) and emptying of the artery. Both events will lead to a rapid increase of the evaporator temperature. During the current tests, the secondary screen and the artery were simultaneously observed when the heat input approached the transport limit. In the majority of the tests, the artery emptied suddenly when the transport limit was reached. Being deprived of its supply of liquid, the secondary screen then rapidly dried out and was accompanied by a sharp rise in evaporator temperature.

On two occasions, however, the opposite sequence was observed. The secondary screen dried out upon reaching the transport limit. Simultaneously, the evaporator ΔT increased. The artery remained filled even after increasing the heat input substantially above the drying and burnout limit of the secondary screen. If thermocouples had been the only instrumentation (as with a metal heat pipe) this burnout mechanism would have been interpreted as a failure of the artery since the temperature profile was similar to that during an artery failure.

The above described phenomenon -- i.e., secondary wick failure prior to artery failure -- was also investigated analytically. It was found that, with the current design, the heat transport capability is indeed limited by the secondary wick and its dryout before artery failure should be the rule rather than the exception.

Quantitative test results of transport limitation and thermal gradients with methanol as the working fluid are presented in Figures 3.4 through 3.6. Figure 3.4 represents the maximum heat transport versus evaporator elevation. These data points were obtained by three different types of tests:

- Setting the heat pipe at a specific tilt with a puddle below the artery and gradually increasing the power.

- The same as above except there was no puddle below the artery.
- Applying a specific power in the horizontal position (with no puddle) and gradually raising the evaporator.

In addition to the test results, Figure 3.4 also gives the theoretical capability of the artery alone and of the artery in combination with the circumferential secondary wick. The agreement between experimental data and calculation is fairly good considering the uncertainty in the permeability of a single layer of screen. The important result is that the heat transport capability of this arterial heat pipe design is controlled by the secondary wick rather than by the artery. In order to fully realize the potential of composite wick heat pipes the secondary wick must be optimized along with the artery.

Figure 3.5 presents the measured evaporator temperature drop as a function of the heat input. The plotted temperature drop is the difference between the evaporator wall temperature and the vapor temperature. The data is fairly consistent and yields for an evaporator area of 45.5 cm^2 and a calculated evaporator film coefficient of 0.136 Watt/$cm^2\,^oC$. The film coefficient corresponding to a 0.125 mm thick liquid layer of methanol (200-mesh screen) is calculated to be 0.153 Watt/$cm^2\,^oC$.

Figure 3.6 presents the condenser thermal gradient as a function of the evaporator heat input. Although several series of tests indicate the same slope, the temperature drop at zero power is always finite and different for each test series. This difference is due to the changing cooling water inlet temperature and flow rate which was not controlled very accurately. Thus, the heat gain from the surrounding room temperature was substantial and varying between test series. The condenser film coefficient calculated from these data is approximately 0.31 Watt/$cm^2\,^oC$.

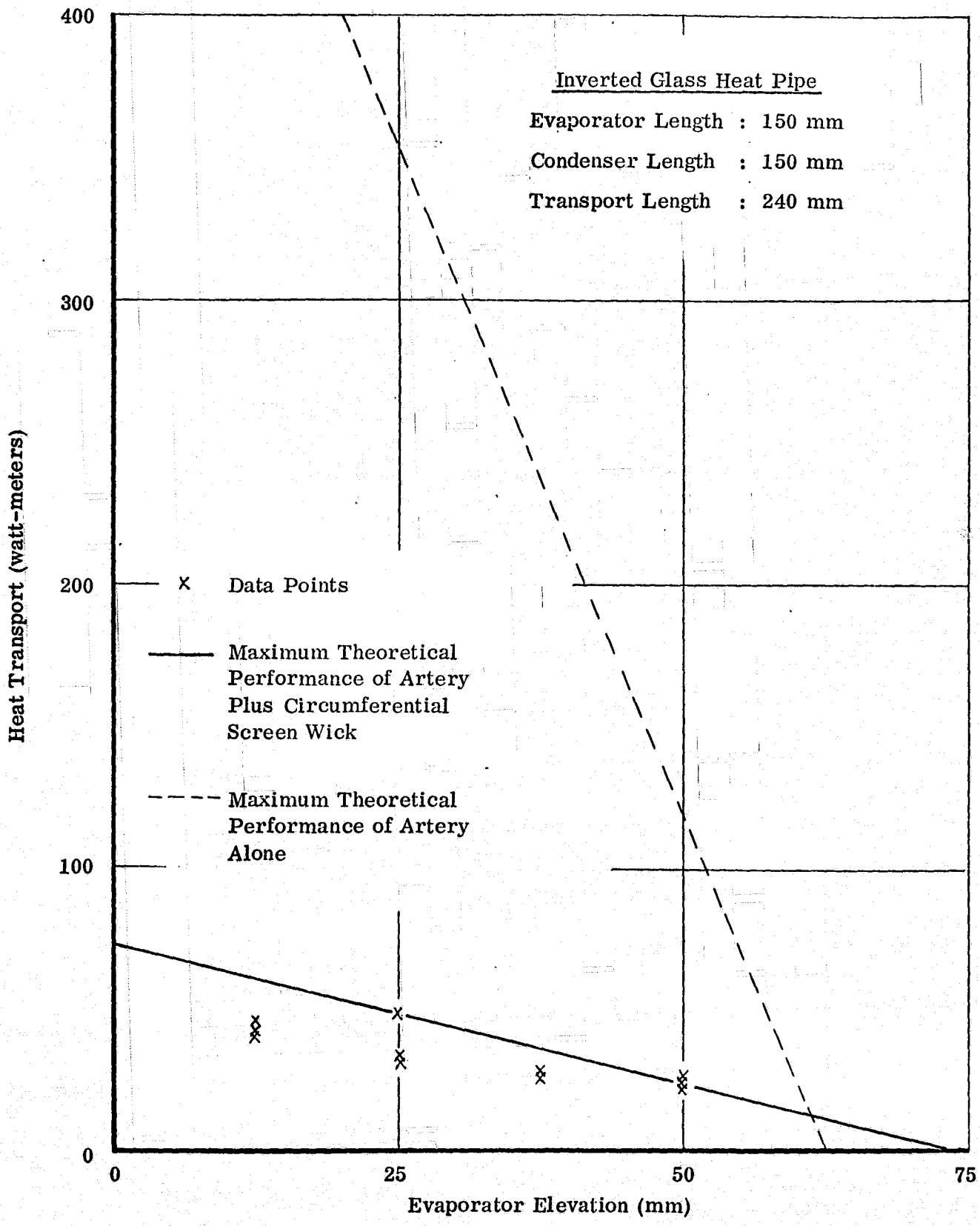

FIGURE 3.4

HEAT TRANSPORT OF INVERTED GLASS HEAT PIPE VS. EVAPORATOR ELEVATION

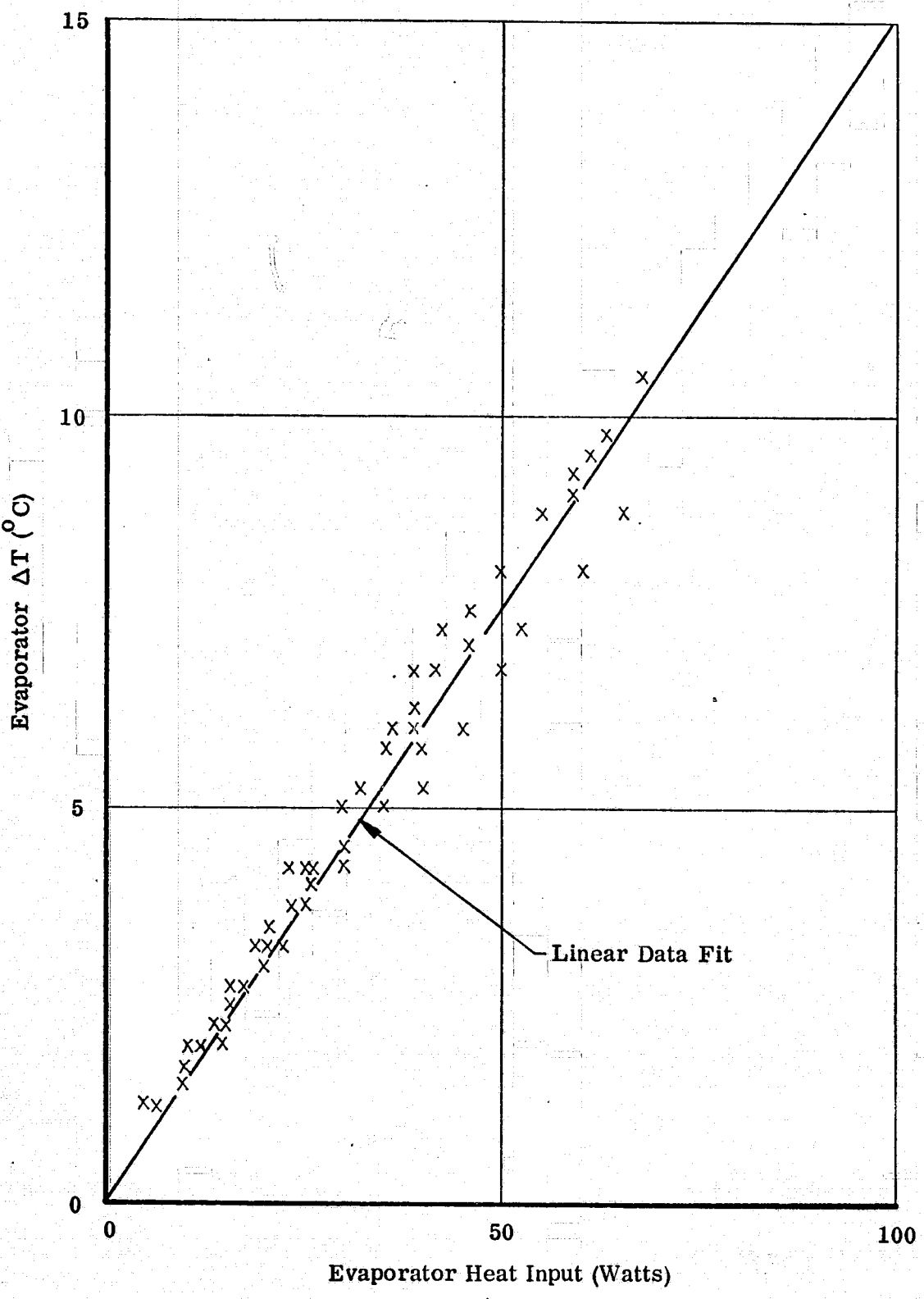

FIGURE 3.5

EVAPORATOR TEMPERATURE DROP OF
INVERTED GLASS HEAT PIPE

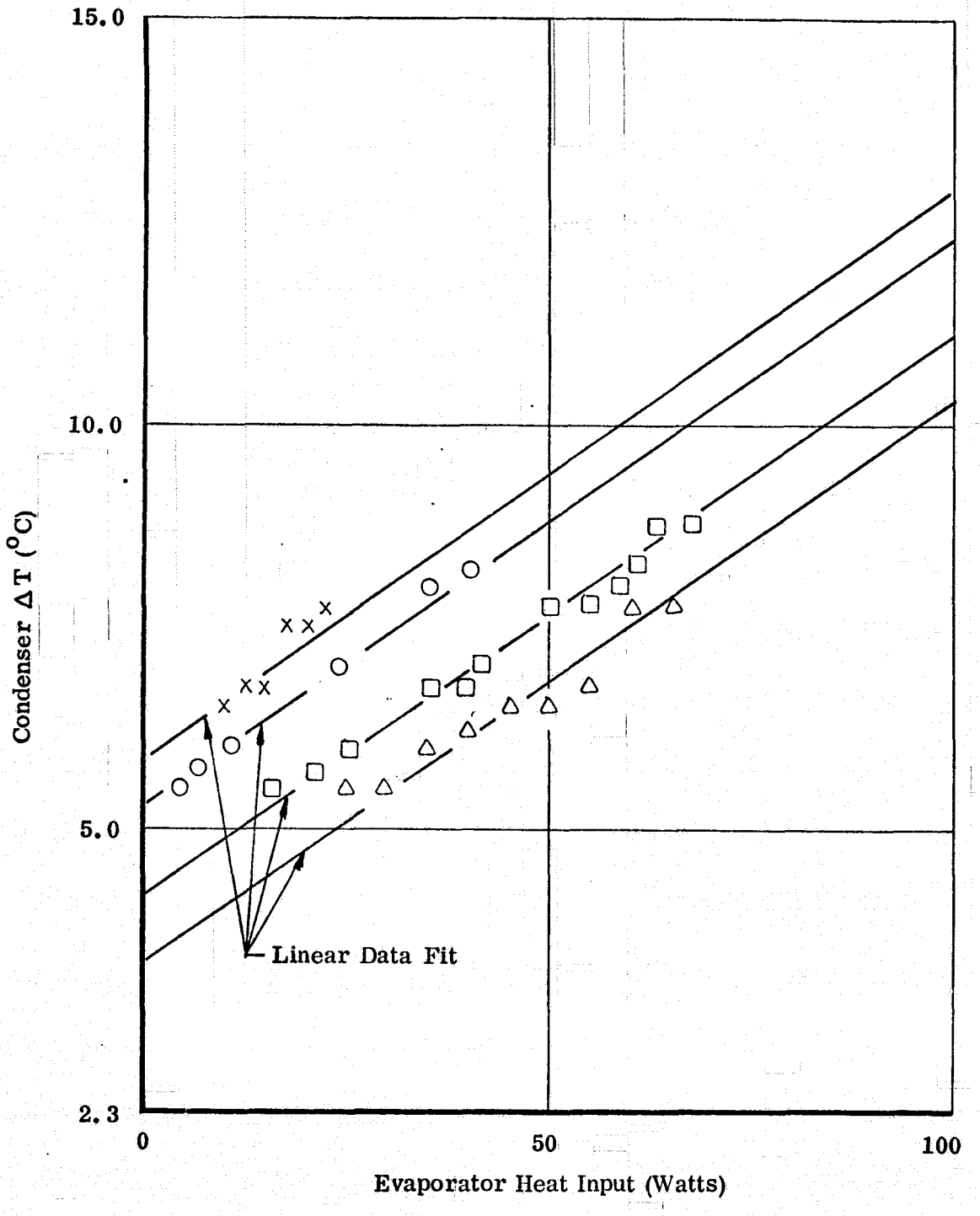

FIGURE 3.6

CONDENSER TEMPERATURE DROP OF
INVERTED GLASS HEAT PIPE

In addition to the priming experiments described above, filling of the artery by condensation was investigated. The complete wick (both secondary and primary) was dried out over the total length. A heater blanket was wrapped around the fluid reservoir which contained all the methanol. When heat was applied to the reservoir, the methanol vapor traveled to the cooler wick. As a result, the secondary wick eventually wetted completely. However, the artery itself did neither wet nor fill with fluid.

Motion pictures were taken by GSFC personnel of the glass heat pipe during its operation with methanol. Included in these 16 mm movies were both normal speed (24 fps) and slow motion (64 fps) sequences of the arterial wick operating during the priming and depriming phases. These movies were taken through a zoom lens which could only focus down to 1.5 m. Both phases of wick operation (priming and depriming) were clearly recorded. During priming, the gradual collapse of a vapor bubble could be observed. During depriming, a bubble grows extremely fast and occupies almost instantaneously the visible section of the artery. Because of the poor focusing, it was not possible to determine whether the secondary wick dried prior to or after the artery deprimed.

3.2.2 Methanol Working Fluid - Screwthread Secondary Wick

Toward the end of the program, the single layer screen secondary wick was replaced by screwthread grooves. A screwthread consisting of 38 grooves per centimeter was machined onto the surface of the inner tube in the evaporator section of the heat pipe. The same single layer artery which was used with the screen secondary wick was spot-welded to the externally grooved tube.

One objective of the testing was to observe the filling and draining of the grooves during various modes of operation. Unfortunately, direct observation proved difficult since filled and dry grooves could hardly be distinguished. Filling of the grooves could

be observed, however, whenever they were initially completely dry. While lowering the evaporator from a high elevation toward the horizontal the filling of the grooves occurred stepwise beginning from the downstream end of the evaporator and proceeding toward the upstream end. Each individual groove filled very fast; some of them filled as a group, and occasionally one or a few were skipped and filled later and out of sequence. It is believed that the somewhat irregular nature of the filling process is due to nonuniformities in the artery attachment. The only source of liquid available to the grooves is the fillet between the artery and the threaded tube. The local size of the fillet depends on the contact between artery and threaded tube and may vary along the length of the evaporator. Drying out of the grooves could not be observed with a transparent liquid such as methanol.

A second objective of the tests was to obtain quantitative data for the evaporator film coefficient for various fill conditions of the grooves. But since the liquid contained in the grooves was not observable the correlation could not be performed. Therefore, the tests were directed at studying the burnout characteristics at various evaporator elevations. During the tests, the secondary wick and the artery were observed simultaneously as the heat input was increased gradually until the artery deprimed (i.e., a bubble formed in the artery and grew in length. Quantitative test results for the maximum measured heat transport capability and thermal conductances are presented in Figures 3.7 and 3.8. Figure 3.7 shows the burnout heat input versus evaporator elevation and Figure 3.8 the temperature drop at the evaporator versus power input. The results in Figure 3.7 indicate that the artery has a static wicking height of approximately 7.5 cm and a maximum heat transport capability ($\dot{Q}\ L_{eff}$) of 1780 Watt-cm at horizontal orientation. The measured static height is very close to the predicted height of 7.3 cm for the combination of 200-mesh screen and methanol. But the transport performance is very poor in spite of the fact that the artery

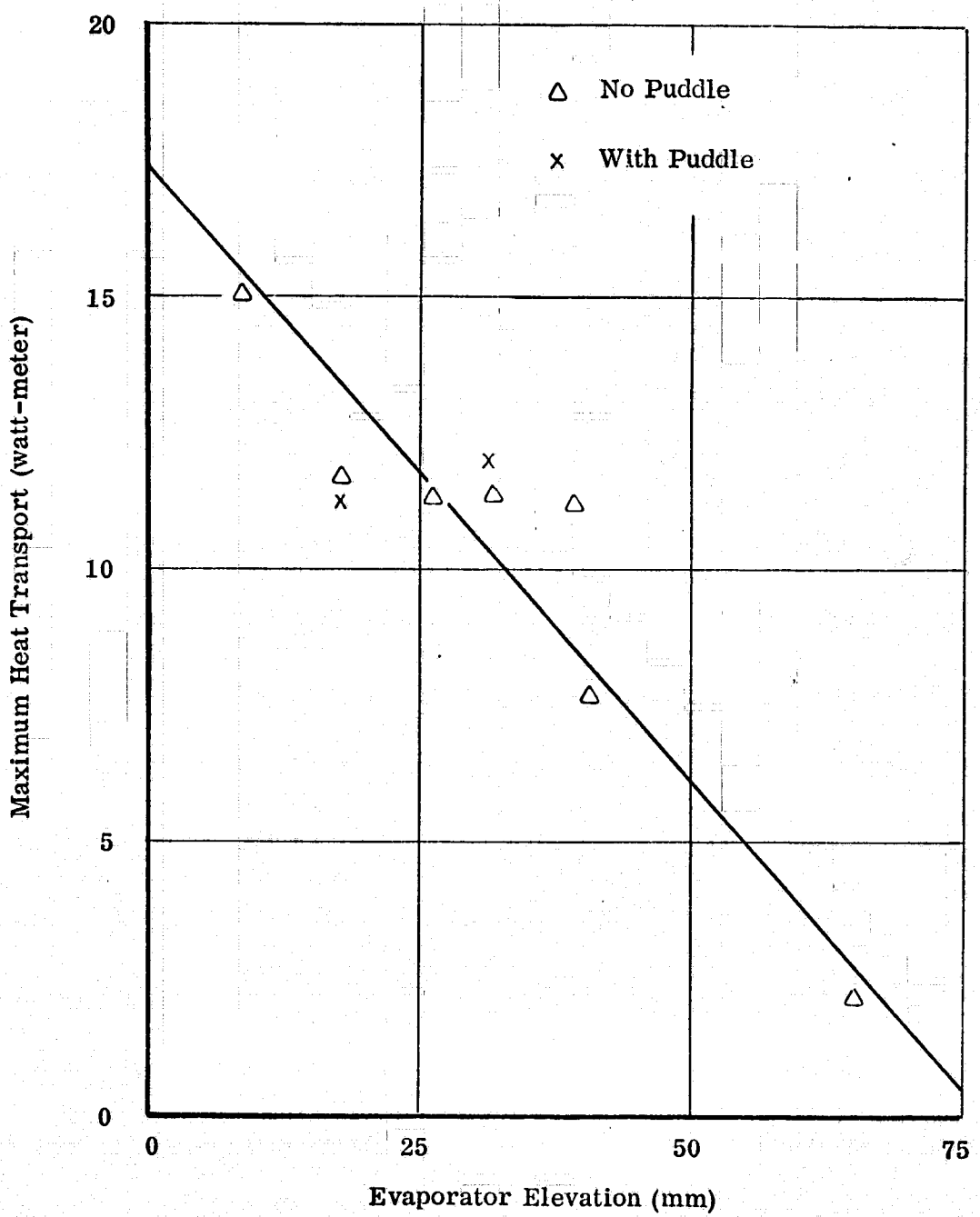

FIGURE 3.7

HEAT TRANSPORT CAPABILITY OF INVERTED GLASS HEAT PIPE WITH SCREWTHREAD GROOVES AND PEDESTAL ARTERY

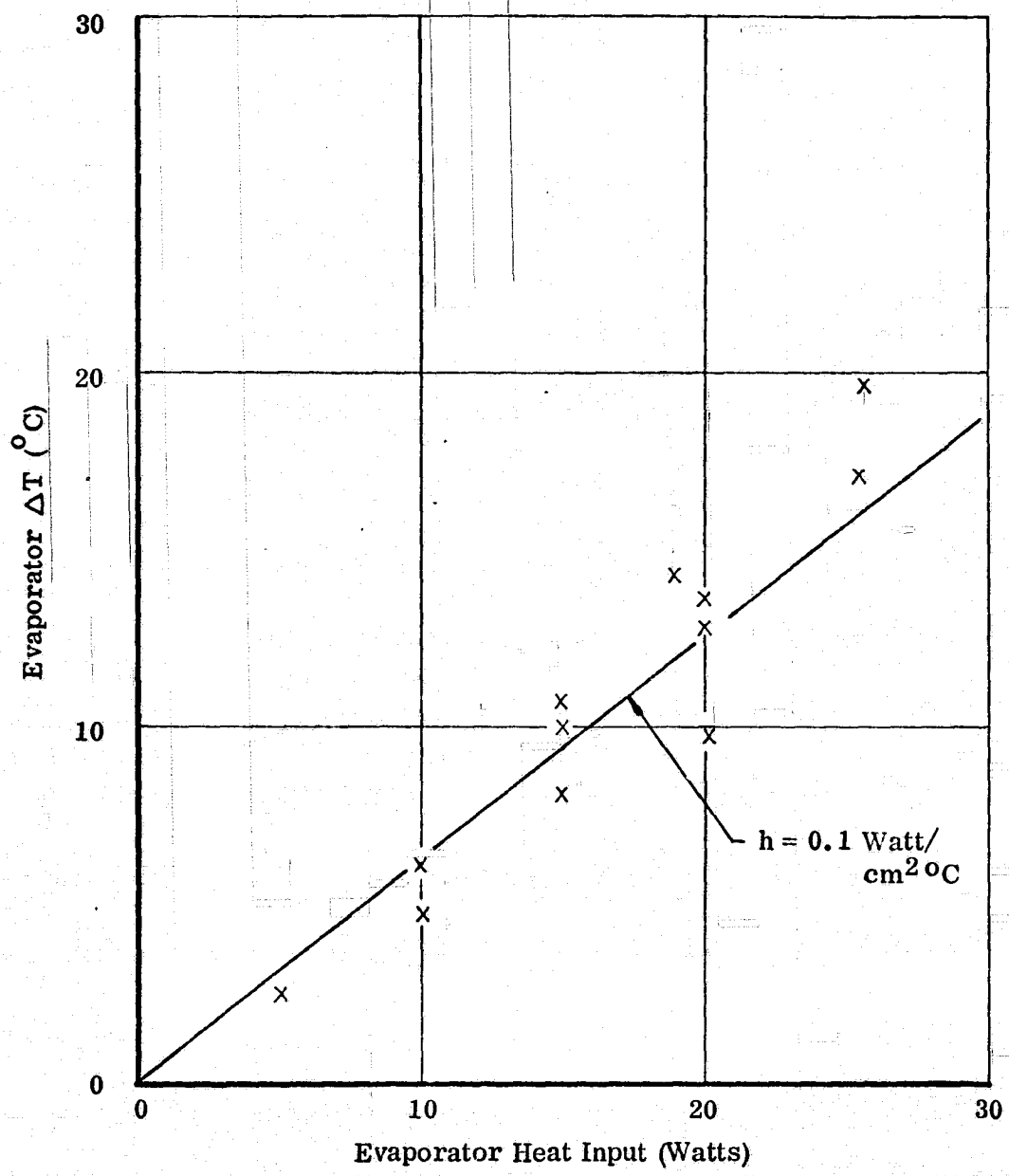

FIGURE 3.8

EVAPORATOR TEMPERATURE DROP OF INVERTED GLASS HEAT PIPE
WITH CIRCUMFERENTIAL GROOVES AND SECONDARY WICK IN EVAPORATOR

has its maximum static pumping capability. This behavior indicates that the transport of this system is probably controlled by the secondary wick (grooves) rather than by the artery. The calculated evaporator film coefficient based on the data shown in Figure 3.9 is 0.1 Watt/cm^2 ^{o}C. By comparison, the corresponding value obtained with one layer of 200-mesh screen as the secondary wick was 0.135 Watt/cm^2 ^{o}C. The lower evaporator film coefficient may be due to experimental error or, more likely, to partial groove dryout which would be in agreement with the low axial transport capability.

Although visual observation of groove dryout was not possible, the analytical model tends to confirm that the performance of the heat pipe was limited by the grooves. Figure 3.9 gives the predicted axial heat transport capability in "zero g" as a function of evaporator heat flux based on the actual groove geometry (see Section 2 for a discussion of the model). This figure shows a maximum permissible evaporator heat flux of 2.5 Watt/cm^2 and a rapid deterioration of the axial transport capability of all heat fluxes greater than 0.5 Watt/cm^2. The actual heat flux at the horizontal orientation was 1.0 Watt/cm^2. Thus, at least a partial dryout of the grooves at the applied heat inputs appears probable and the low transport capability is not unreasonable.

3.2.3 Ammonia Working Fluid - Single Layer Screen Secondary Wick

Before testing the inverted glass heat pipe with ammonia, the entire system was proof pressure tested to 20 atmospheres which is equivalent to operation with ammonia at 52^{o}C. All actual testing was performed at less than 25^{o}C.

Emphasis during testing was on the priming mechanism. As with methanol, two procedures to prime the artery were studied. The first approach was to prime when the artery was partially filled but when the 200-mesh wall was completely wetted. Priming of this completely wetted artery was never accomplished. Attempts have been made to

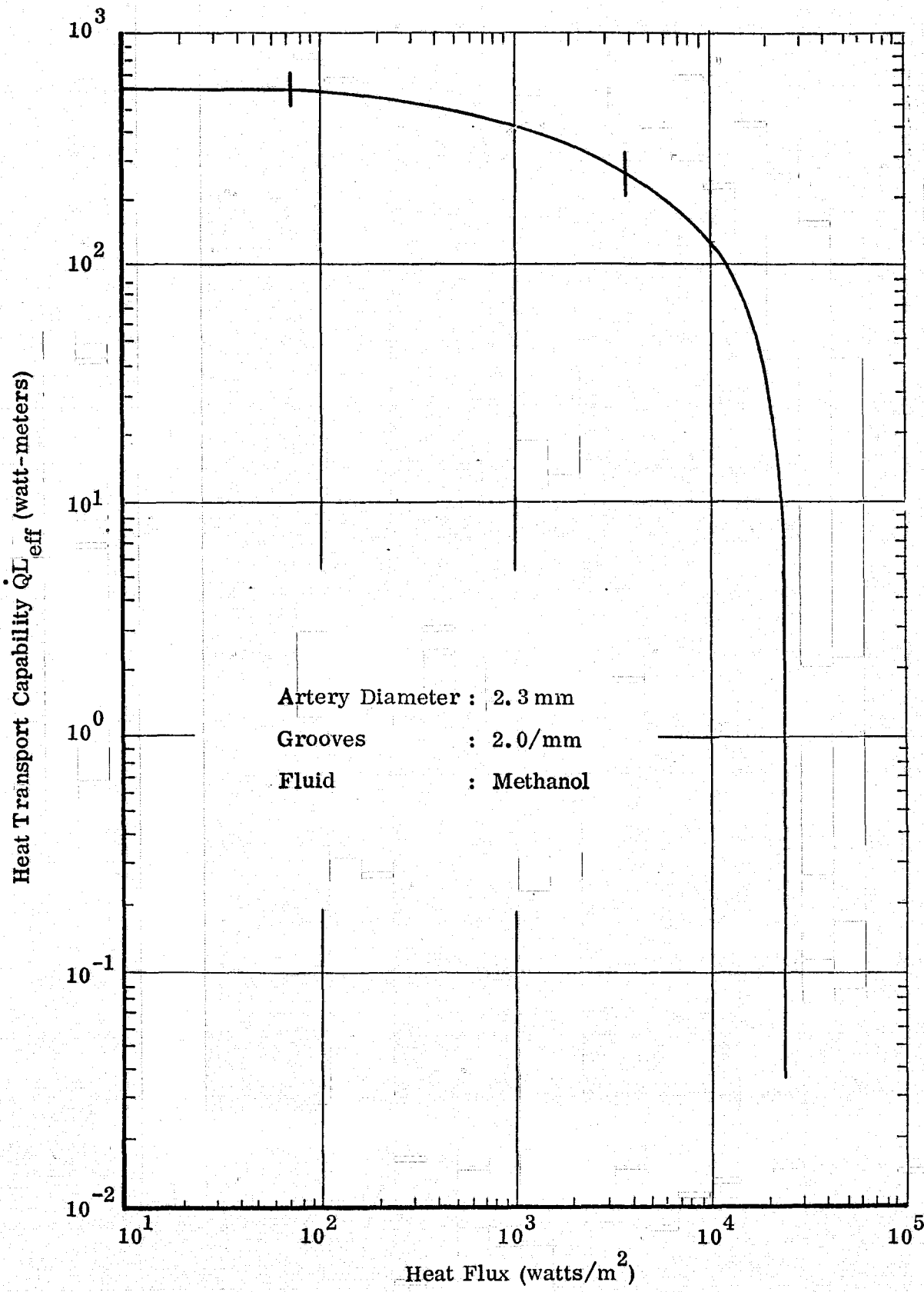

FIGURE 3.9

PREDICTED HEAT TRANSPORT CAPABILITY
OF INVERTED GLASS HEAT PIPE

to prime in this mode with and without power applied. With no power, a vapor slug remains in the artery. With power added to the evaporator, the vapor slug flows to the hottest spot of the evaporator and then grows in length.

The second method of priming has been successful. This approach consists of intentionally drying out the evaporator artery walls at a large elevation by applying some heat before initiating the priming procedure. After the artery and secondary wick are dried out, the power is shut off and the tilt of the heat pipe is adjusted so that evaporator is elevated approximately 5 mm. The heat pipe is then maintained at this elevation for a few minutes until the temperatures along the artery are almost uniform. Priming is then achieved as the evaporator is lowered to slightly below the horizontal. At least partial priming by this method has been accomplished repeatedly in the tests.

Priming with power applied was unsuccessful even from a dried-out condition. With as little as 5 watts applied, a bubble would form and grow in the evaporator as the liquid advanced to that section. The formation of this bubble prevented further priming of the artery. The same configuration had been primed repeatedly from a dried-out condition with as much as 35 watts applied when methanol was used as a working fluid. The vapor pressure of ammonia is approximately two orders of magnitude greater than that of methanol. Consequently, a small temperature difference will result in a substantially larger pressure difference in ammonia. This larger pressure difference may be what is causing the bubble to grow and preventing priming in the ammonia system.

Once the artery was primed, tests were conducted to study the burnout characteristics at various evaporator elevations. During the tests, the secondary wick and the artery were observed simultaneously as the heat input was increased gradually until burnout occurred. During burnout, the artery and secondary wick seemed to dry simultaneously.

Heat transport data were obtained with and without a puddle of excess fluid in the inverted glass pipe. Although the data is limited, higher heat transports were generally achieved in the absence of a puddle. It is possible that splashing of the puddle due to local boiling causes the artery to deprime before the capillary limit is reached.

3.3 Retesting of OAO-C Level 5 Heat Pipe

Performance tests were conducted with the Qualification Model of the OAO-C Level 5 heat pipe. The design of this pipe is described in detail in Reference 8. Basically, it is an Al/NH_3 heat pipe with a 2.3 mm diameter pedestal artery formed from 200-mesh stainless steel screen. Circumferential distribution of the working fluis is accomplished through spiral grooves in the wall of the 1.27 cm diameter heat pipe (19 grooves/cm).

The objective of this retesting was twofold:

- To determine the ultimate axial heat transport capability at various elevations; and
- To evaluate the performance of the circumferential grooves, in particular, in the evaporator area.

The second objective is of particular interest for this program. The analytical model which is described in Section 2 correlates the axial transport capability with the heat flux at the evaporator. The OAO-C heat pipe, because of its length, appeared to be a good vehicle to test that theoretical model.

The test setup is shown in Figure 3.10. Heat was applied over a 20 cm section between saddle C and D and removed from a bath at saddle B. This configuration was chosen in order to realize a large effective transport length of 300 cm. (A slightly larger

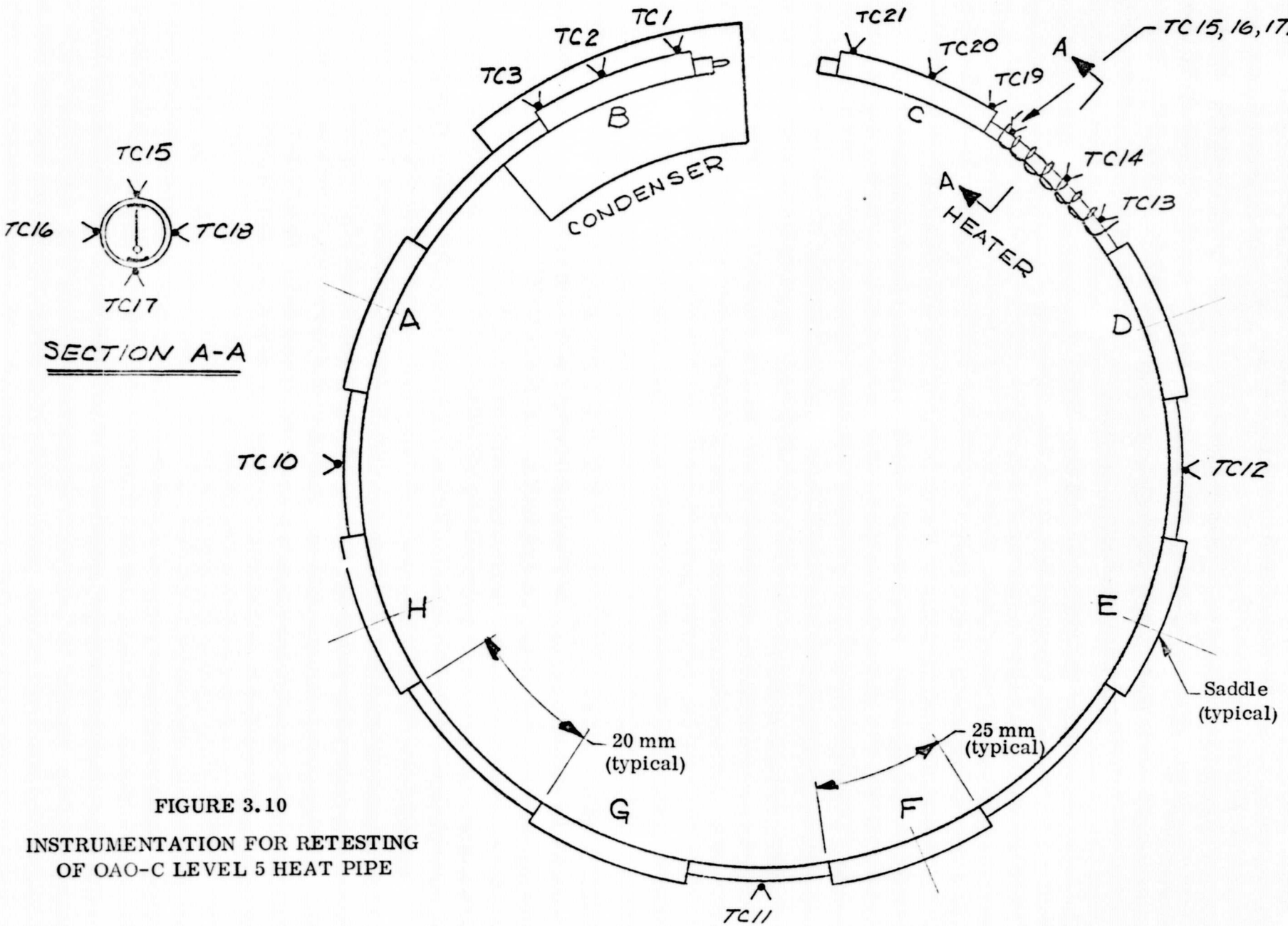

FIGURE 3.10

INSTRUMENTATION FOR RETESTING
OF OAO-C LEVEL 5 HEAT PIPE

effective length could have been achieved by applying heat to saddle B, but the conductance of the saddle tends to obscure circumferential temperature gradients.) Also shown in Figure 3.10 is the location of the thermocouples. At one point on the evaporator, four (4) thermocouples were placed 90° apart around the heat pipe in order to detect circumferential temperature differences.

Tests were conducted with the condenser immersed in an ice bath. The vapor temperature of the heat pipe ranged from 5°C to 30°C depending on the heat load. No attempts were made to investigate reliable priming techniques during this series of tests. Once the artery had been primed, the tests were conducted with the objective of studying ΔT's and maximum axial heat transport.

The test sequence was as follows. At a given elevation, heat was applied to the resistance heater in increments of 50 watts up to a maximum of 250 watts which was the limit for that heater. If no burnout was noticed the elevation of the evaporator was increased and the procedure repeated. Tests were conducted with the following evaporator elevations: 1.35 cm, 2.47 cm, 3.23 cm, 4.30 cm, 5.14 cm, 6.07 cm, and 7.14 cm. The only burnout which was reached occurred at an elevation of 7.14 cm and an input power of 250 Watts. (The artery was still primed at 7.14 cm and 200 watts.)

The theoretical transport capability of this particular artery along with two experimental points just prior to burnout are shown in Figure 3.11. The theoretical curve is based on the flow resistance of the artery alone; i.e., neglecting the effects of the secondary wick (bridges and grooves). This approach seems justified in view of the fact that the secondary wick was completely dried out (see below). The agreement between theory and experiment is fairly good considering that the artery diameter is not precisely known, although the performance is sensitive to its fourth power.

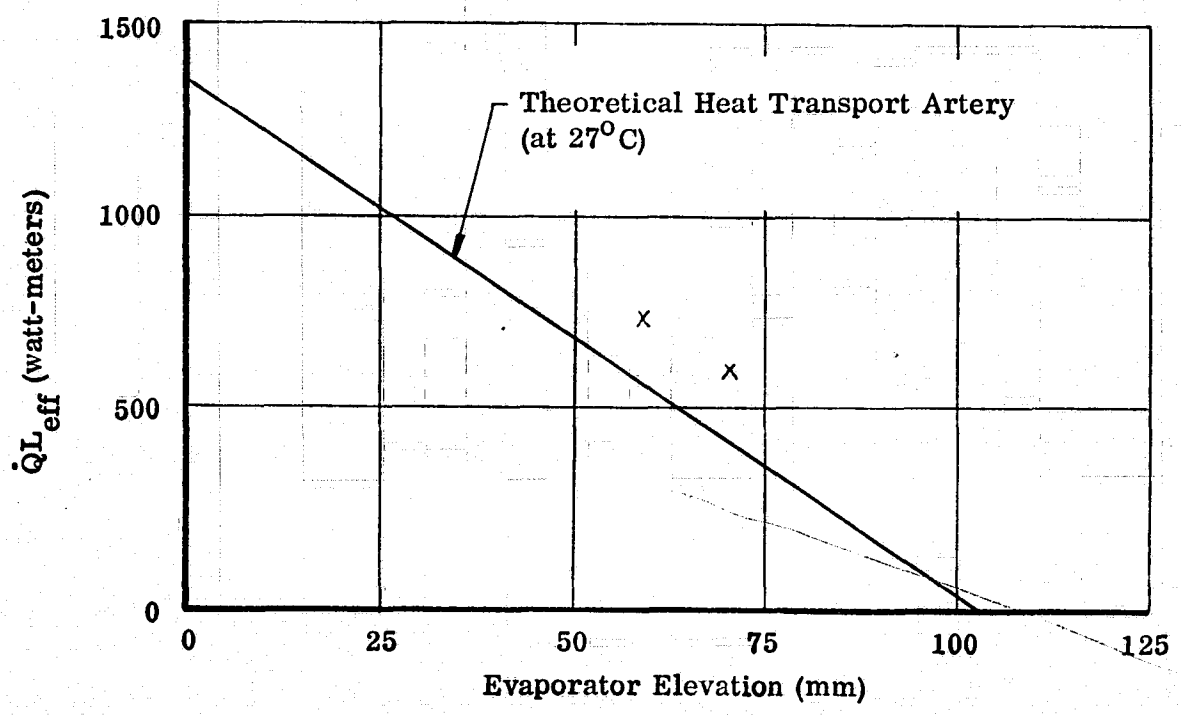

FIGURE 3.11

THEORETICAL AND EXPERIMENTAL TRANSPORT CAPABILITY OF OAO PEDESTAL ARTERY

The temperature distribution along the heat pipe yielded some interesting results about the performance of the evaporator grooves. The evidence appears conclusive that the evaporator grooves were dried out at all input powers and elevations, in spite of the artery being primed all the time. The average temperature difference between the evaporator and the adiabatic section is shown in Figure 3.12 as a function of input power for various elevations. Since all curves approximate very closely a straight line, one must conclude that either the grooves were properly filled at all times or always dried out. The magnitude of the ΔT's precludes the first possibility. This is further demonstrated in Figure 3.14 in which the effective film coefficient is plotted versus elevation. The low film coefficients of 0.1 - 0.15 Watt/cm^2 $^\circ$C virtually rule out the possibility that the grooves were filled during these tests. If one assumes that the grooves are completely dry, then the input heat would have to be conducted around the tube to the point where the artery and its pedestal are located. An "effective" film coefficient can be calculated based on this model. The result is indicated in Figure 3.13 which further substantiates the findings that the grooves were completely dry.

It was mentioned earlier that the heat pipe was instrumented to detect circumferential temperature gradients. These measurements were, however, completely inconclusive. No systematic differences appeared to exist between the thermocouples near the top, the sides, or the bottom of the heat pipe. The ΔT's, which are plotted in Figure 3.12 are therefore based on the average evaporator temperature.

Examination of Figures 3.12 and 3.13 shows that the evaporator ΔT and the effective film coefficient are somewhat dependent on the evaporator elevation. The ΔT increases and the effective film coefficient decreases with evaporator elevation. This effect has been observed before but has never been explained satisfactorily.

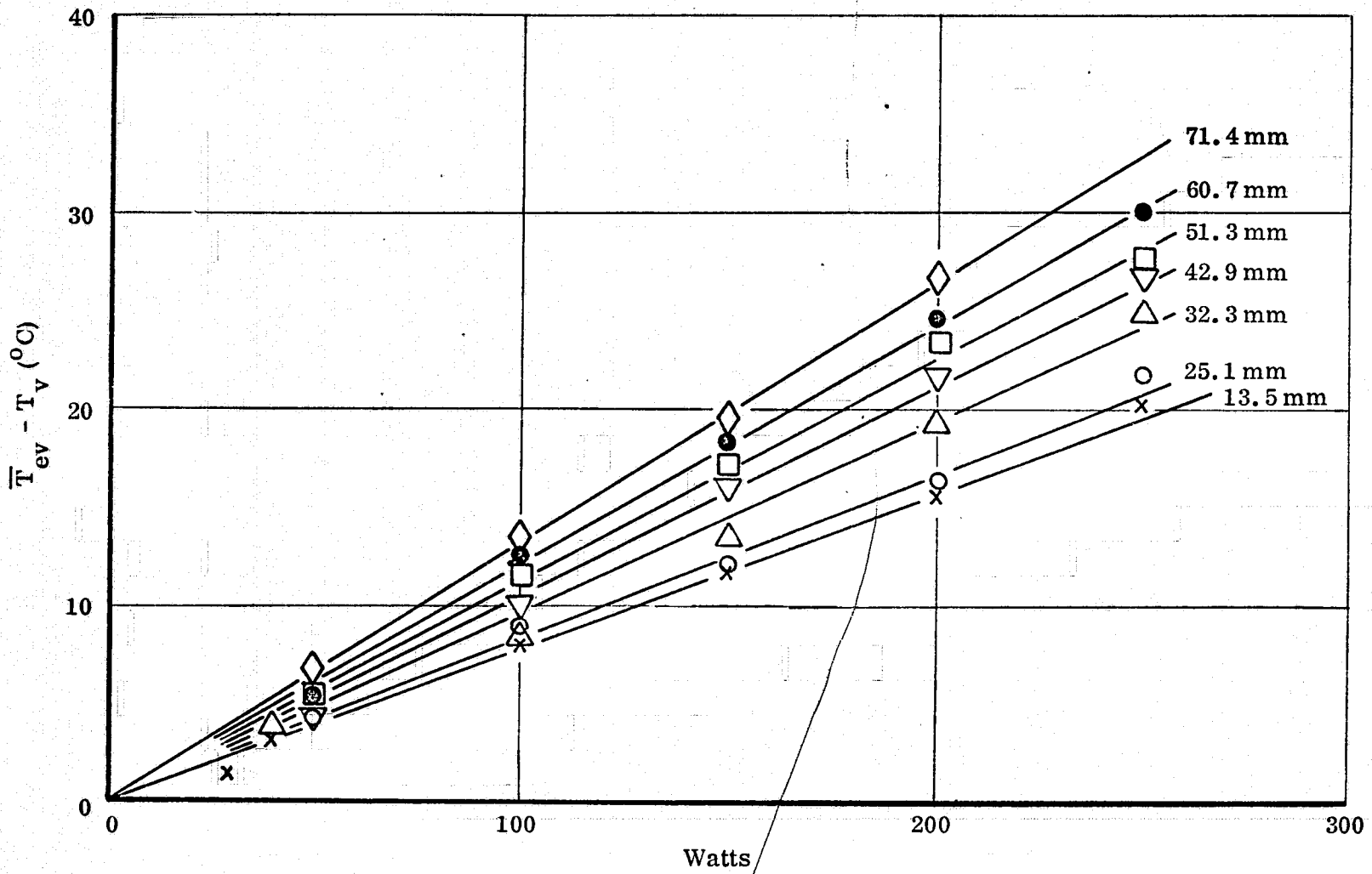

FIGURE 3.12

EVAPORATOR TEMPERATURE DROP OF OAO-C PEDESTAL ARTERY HEAT PIPE

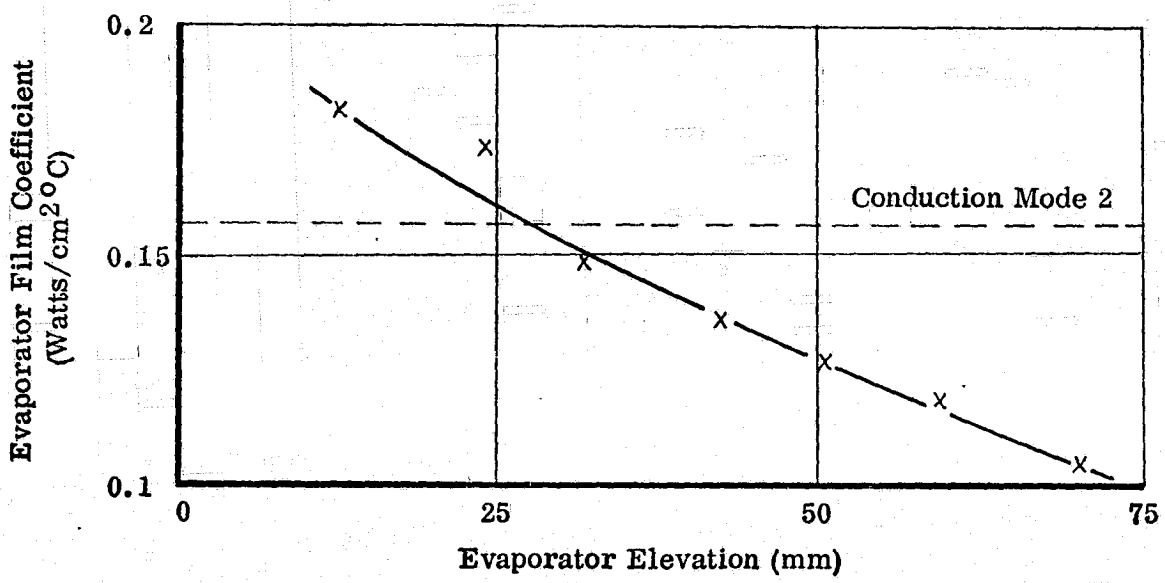

FIGURE 3.13

EFFECTIVE EVAPORATOR FILM COEFFICIENT
OF OAO-C PEDESTAL ARTERY HEAT PIPE

One of the objectives of these experiments was to test the analytical model. The model predicts the maximum axial heat transport capability as a function of evaporator heat flux. In Figure 3.14 this maximum heat transport, as given by the model, is plotted as a function of evaporator heat input. Also plotted in this figure is the normalized heat transport for the various experimental heat inputs. Examination of this figure shows that above 74 watts input the experimental transport requirement exceeded the capability of the combination of artery and grooves. The grooves are therefore expected to dry out which is confirmed by the low effective film coefficients. Below 74 watts input the grooves should be filled. Close examination of the ΔT_e versus $\dot{Q}$ plot for 1.35 cm elevation (Figure 3.12) shows that for very low $\dot{Q}$'s the data points deviate from the straight line indicating a higher effective evaporator conductance.

The measured heat transfer at the condenser is shown in Figure 3.15. The condenser ΔT's are independent of elevation and much smaller than at the evaporator. Based on the slope of the ΔT_c versus $\dot{Q}$ plot an effective film coefficient of 1.5 Watts/$cm^2{}^oC$ was calculated.

In summary, the retesting of the OAO-C heat pipe yielded a maximum axial transport capability of 75,000 Watt-cm at 6 cm elevation and 60,000 Watt-cm at 7 cm elevation. The predicted capability in "zero g" is 138,000 Watt-cm. In order to achieve these transport capabilities experimentally with heat applied over a 20 cm section, the evaporator heat flux exceeds the limit for circumferential distribution and the grooves at the evaporator run dry.

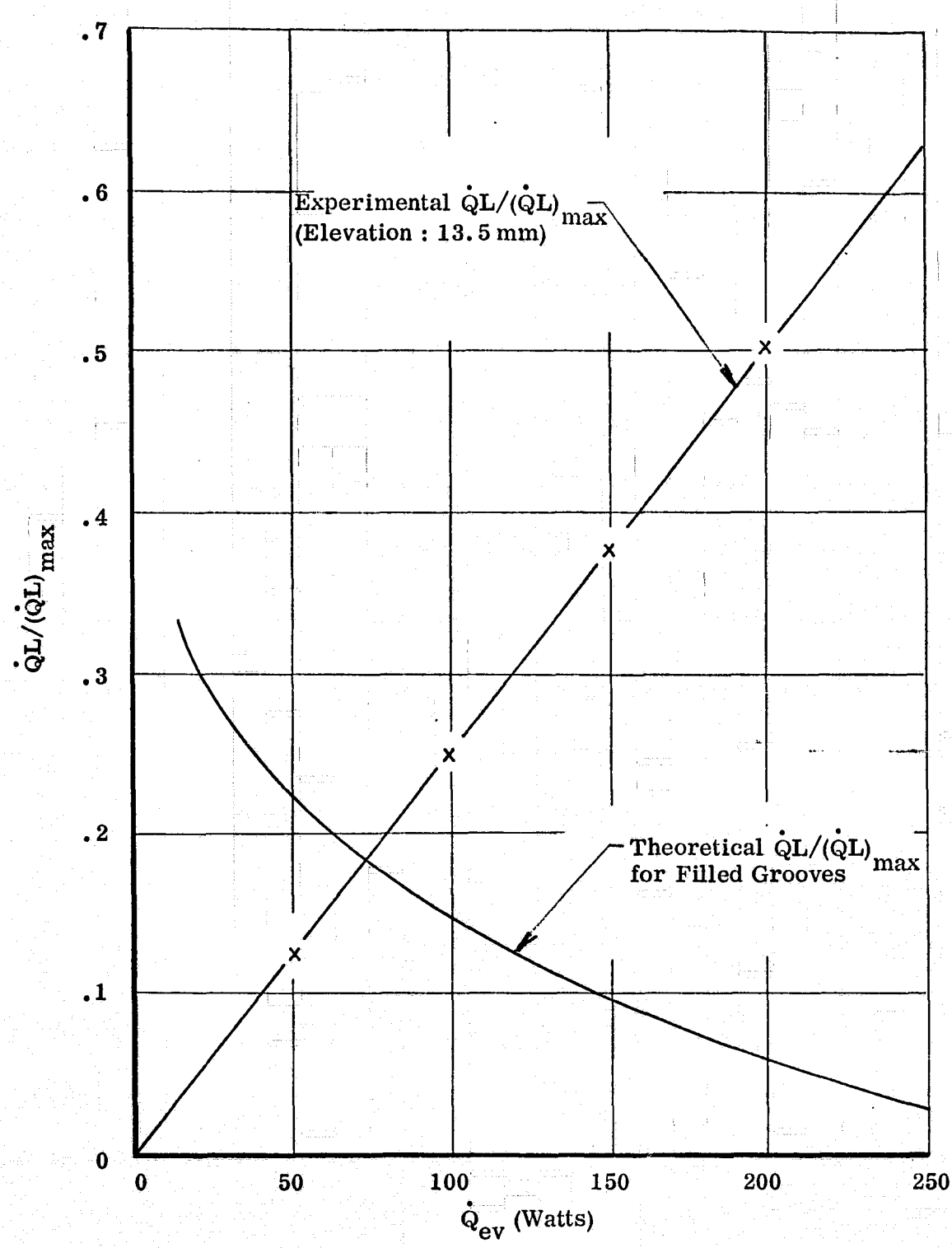

FIGURE 3.14

THEORETICAL AND EXPERIMENTAL $\dot{Q}L/(\dot{Q}L)_{max}$
AS A FUNCTION OF EVAPORATOR HEAT INPUT
(The Theoretical Curve Defines the Upper
Limit for which the Grooves Remain Filled)

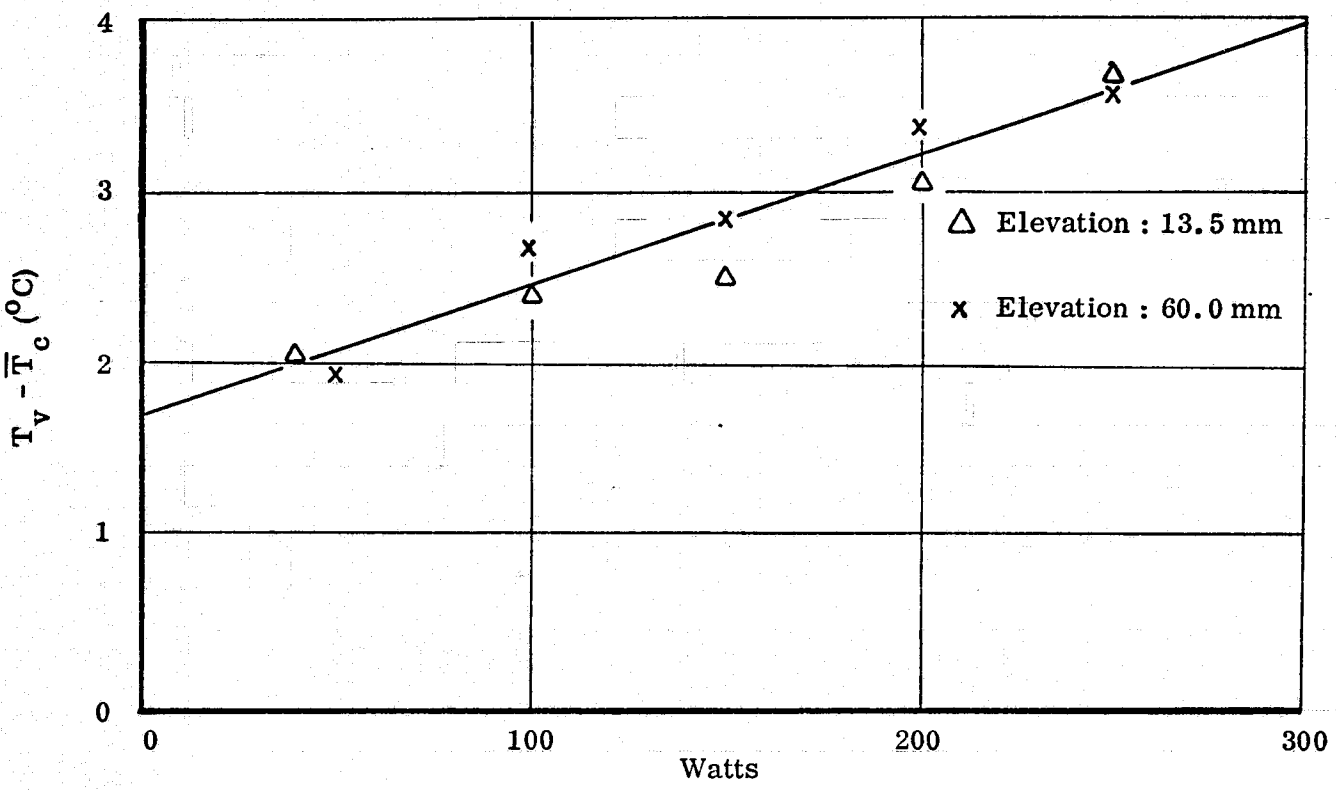

FIGURE 3.15

CONDENSER HEAT TRANSFER

4. REFERENCES

1. "Experimental High Performance Heat Pipes for the OAO-C Spacecraft," by W. Bienert and E. Kroliczek, ASME Paper 71-Av-26, July 1971

2. "The Development of a 150,000 Watt-Inch Variable Conductance Heat Pipe for Space Vehicle Thermal Control," ASME Paper 72-ENAv-14, May 1972

3. "Development of a Self-Priming High Capacity Heat Pipe for Flight on OAO-C," by F. Edelstein, et al, presented at the AIAA Thermophysics Conference, April 1972

4. "Feasibility Study and Development of a Constant Temperature Heat Pipe System," by M. Groll and P. Zimmerman, Phase I Final Report under ESTEC Contract No. 1703/72 SK, November 1972

5. "High Reliability Heat Pipes," by B. Marcus, presented at NASA Heat Pipe Technology Meeting at GSFC, January 1973

6. "Heat Pipe Capability Experiments," by J. Kemme, Los Alamos Scientific Laboratory Report LA-3585-MS, October 1966

7. "Ames Heat Pipe Experiment (AHPE) Description Document," by B. Marcus, NASA Report CR-114413, January 1972

8. "Fabrication and Qualification of Two Circular Heat Pipes for OAO-C," Dynatherm Corporation, Report No. DTM-70-7, October 1970

9. "Heat Pipe Design Handbook," Part I, prepared for NASA-MSC by Dynatherm Corporation, August 1972